Comparison of Dipole Antenna Designs for the LWA

Aaron Kerkhoff (ARL:UT)

August 25, 2007

1 Introduction

This report provides a comparison of a number of dipole antenna element designs, which could be used in the LWA. The antenna designs considered include the inverted-V dipole which is being used as the low band antenna element in LOFAR, the wire-frame bow-tie dipole being used in the MWA low-frequency demonstrator (LFD), and the blade and fork dipoles, which are candidate designs for LWA. The designs not currently being considered for use in the LWA have been scaled in size to operate at LWA frequencies to simplify comparison. Other than scaling the size of some, no attempt has been made to optimize the performance of any of the antenna designs considered. Rather, the purpose of this report is to compare the basic properties of these different designs.

NEC2 was used to simulate the performance of each antenna. A number of metrics were then calculated from the simulation results. These include sky noise frequency response, radiation pattern quality including beamwidth and axial ratio, effective collecting area at the zenith, and reception of vertically polarized incident fields at the horizon. Though also important, neither the mechanical complexity nor the monetary cost of each design are considered explicitly in this report. Scripts were written to automate the generation of NEC antenna models, execution of NEC2, generation of all plots and figures, and generation of LaTeX code to insert them into this report. Once written, these scripts enabled rapid evaluation of each antenna design for different sets of design parameters.

Some basic assumptions are made in order to simplify the analysis. First, all antennas are assumed to operate over an infinite, perfectly conducting ground. Additionally, only the performance of a single dipole in isolation is considered. That is, no mutual coupling effects are included in the results.

The organization of this report is as follows: first, all of the performance metrics considered are defined. A description of the antenna geometry and the calculated metrics are provided in separate section for each antenna design. Then, a comparison is made between all of the designs considered for each metric. Finally conclusions are given.

2 Definitions

Each of the performance metrics considered in this study are defined in this section. The formats used to report each of the metrics are also described.

The equivalent sky noise temperature received by a lossless antenna, T_{SKY}, is estimated using the expression for Galactic background emissions in the Galactic polar regions given by Cane [1]. The

sky noise temperature of a real antenna is then given by

$$T_{ANT} = T_{sky}\frac{(1-|\Gamma|^2)}{L_g} \tag{1}$$

where Γ is the reflection coefficient of the antenna, $(1-|\Gamma|^2)$ is mismatch loss efficiency, and L_g is ground loss. Since an infinite perfectly conducting ground is assumed in this study, L_g is set to one. T_{ANT} is calculated and plotted as a function of frequency. Results are provided for three different input matching impedances, Z_L = 100 Ω, 200 Ω, and 400 Ω. Additionally, the frequency ranges over which $T_{ANT} >$ 500 K, 1000 K, 1750 K, and 2500 K are calculated and provided in tabular form for each value of Z_L. Given the assumed equivalent noise temperature for the pre-amp, this data can be used to determine the sky to system noise dominance bandwidths achieved with each antenna.

The co- and cross- polarized gain patterns in both the E- and H-planes are calculated and plotted at the frequencies $\{10, 20, 38, 74, 80, 88\}$ MHz; individual plots are made for each frequency. From this data, other metrics are calculated at the same frequencies. The axial ratio of a crossed pair of a given dipole design as a function of observation angle, (θ,ϕ), is estimated using

$$AR(\theta,\phi) = |G_{E,co}(\theta,\phi) - G_{H,co}(\theta,\phi)| \tag{2}$$

where $G_{E,co}$ and $G_{H,co}$ are the co-polarized gain patterns in the E- and H-planes, respectively, of a single dipole expressed in dB. Axial ratio as a function of observation angle is included with the gain pattern plots at each frequency. Additionally, the maximum axial ratio for zenith angles $|z| \leq 74\,^\circ$ is calculated at each frequency and provided in tabular format.

The half-power beamwidths (HPBW) in both the E- and H-planes are calculated at each frequency by $HPBW = 2 * |z_{3dB}|$ where z_{3dB} is defined as follows

$$z_{3dB} = \begin{cases} z|G(z) = G(z=0) + 3dB & \text{if } G_{max} \text{ - G(z=0)} > 3 \text{ dB} \\ z|G(z) = G(z=0) - 3dB & \text{if } G_{max} \text{ - } G_{min} > 3 \text{ dB} \\ z|G(z) = G_{max} - 3dB & \text{otherwise} \end{cases} \tag{3}$$

where G_{max} is the maximum gain and G_{min} is the minimum gain over all z in the given plane. If the maximum gain, which may or may not be at the zenith, (z=0), is within 3 dB of the gain at the zenith, then the HPBW is defined by the zenith angle at which the gain is 3 dB down from the maximum gain (third case above). However, if the gain at the zenith is more than 3 dB below the maximum gain (i.e. there is a "deep" null at the zenith) then the HPBW is defined by the zenith angle at which the gain is 3 dB up from the gain at the zenith (first case above.) Also, if the difference between the maximum and minimum gain is more than 3 dB (i.e. there is a "deep" null between the mainlobe and a sidelobe), then the HPBW is defined by the zenith angle at which the gain is 3 dB down from the gain at the zenith (second case above). These last two cases essentially "penalize" patterns with any nulls not at the horizon deeper than 3 dB. While other definitions of HPBW may be used, this definition was deemed useful as it "flags" patterns exhibiting undesirable deep nulls, which can be a problem with dipole antennas operating at higher frequencies. The pattern data, which is calculated in 3 ° steps is interpolated to estimate HPBW. HPBW data for both planes and for the frequencies $\{10, 20, 38, 74, 80, 88\}$ MHz are provided in tabular form.

Two different methods are used to calculate the effective collecting area, A_e, of an antenna. The first uses the traditional definition of collecting area, which is based upon the gain of the antenna when operated in a transmit mode (that is, the excitation source is placed at the antenna feed)

$$A_{e,rec}(\theta,\phi) = G(\theta,\phi)\frac{\lambda^2}{4\pi}\frac{(1-|\Gamma|^2)}{L_g}. \tag{4}$$

Again, L_g is set to one due to the PEC ground. Effective collecting area is also calculated using the alternate, receive mode-based definition described in [2]. This is calculated in NEC by placing a resistive load Z_L at the feed of the antenna and exciting it by a co-polarized plane wave. The effective collecting area is then calculated by

$$A_{e,tr}(\theta,\phi) = \frac{P_L(\theta,\phi)}{S(\theta,\phi)} \tag{5}$$

$$S = \frac{1}{2\eta_0}|\mathbf{E}|^2 \tag{6}$$

$$P_L = \frac{1}{2}|I_L|^2\mathbf{Re}\{Z_L\} \tag{7}$$

where S is the power density of the incident plane wave, P_L is the power delivered to the load, η_0 is the wave impedance of free space, $\mathbf{E}$ is the incident E-field vector, I_L is the current through the load, and Z_L is the antenna input impedance. In this study, the plane wave excitation is accomplished using the 'EX' card in NEC (assumes a unit magnitude plane wave) rather than by exciting a second, co-polarized antenna placed in the far-field of the antenna under test as described in [2]. Both $A_{e,tr}$ and $A_{e,rec}$ are calculated for z = 0 for input matching impedances values of Z_L = 100 Ω, 200 Ω, and 400 Ω, and plotted as a function of frequency.

Calculations were also performed to determine the sensitivity of each antenna to vertically polarized waves incident from the horizon, which are characteristic of many forms of terrestrial RFI. In order to provide a metric for comparison, the $A_{e,rec}$ calculation is repeated at the horizon for vertically polarized waves in both the E- and H-planes of the antenna. Calculations are performed for input matching impedances values of Z_L = 100 Ω, 200 Ω, and 400 Ω, and plotted as a function of frequency.

A few notes about the results provided below:

- The highest calculated value of cross-polarized component gain in the principal planes for any of the antenna designs considered is < -140 dBi; NEC returned -999.99 dBi for most designs over all frequencies and observation angles. Therefore, cross-polarized gain is not included in the pattern plots below.
- Very low values of $A_{e,rec}$ at the horizon in the antenna H-plane were returned for all antennas. Therefore, sensitivity to vertically polarized waves at the horizon are only reported for the E-plane in the plots below.

3 Thin Wire Inverted-V Dipole

The LOFAR low band antenna, which is designed to operate nominally between 30 to 80 MHz, consists of a crossed pair of thin wire "inverted-V" dipoles as shown in Figure 1. Design information for this antenna was not available at the time this study was conducted, and thus, dimensions were surmised from photos and the operating frequency range. The dimensions of the big blade dipole (see section 6), were used as a starting point. However, in order to make a more fair comparison between the different designs, the length of the wire element (for one arm of dipole), L, was increased from roughly 1.7 m to 1.9 m. This was done so that the electrical length of the wire is roughly equal to that of the blade, which is approximately $L_b + W_b/2$ where L_b and W_b are the length and width, respectively of the blade element. It was then necessary to slightly increase the height of the wire dipole above the ground, H, to 1.6 m so that the elements were not too close to the ground. The droop angle, α, was set to 45 °, and the feed gap, w_f was set to 0.1 m as in the big blade. Since the actual thickness of the wire used in the LOFAR low band antennas is unknown, it was assumed to be relatively thin, with a radius $r_w = 1.5$ mm.

The NEC model used to simulate the inverted-V dipole is shown in 2. The calculated metrics for the thin wire inverted-V dipole are provided in Figures 3-11 and Tables 1-3 in the remainder of this section.

Figure 1: The LOFAR low band antenna [3].

When paired with a lower input impedance value such as 100 Ω, the thin wire inverted-V dipole exhibits a relatively narrow-band response. However, a higher bandwidth can be achieved with this antenna by increasing the input impedance. For example, the bandwidth for $T_{ANT} \geq 1000$ K is increased from 19.6 MHz wide to 39 MHz wide by increasing Z_L from 100 Ω to 400 Ω.

At 38 MHz and below, the radiation patterns of the thin wire inverted-V in both planes exhibit a single, wide beamwidth lobe with the maximum towards the zenith. While a null develops at the horizon in the H-plane, one does not in E-plane, which is an effect of the PEC ground. At higher frequencies, the H-plane pattern maintains its shape and increases in beamwidth up to 80 MHz. By 74 MHz, however, the E-plane pattern develops a sidelobe at the horizon. At 80 MHz

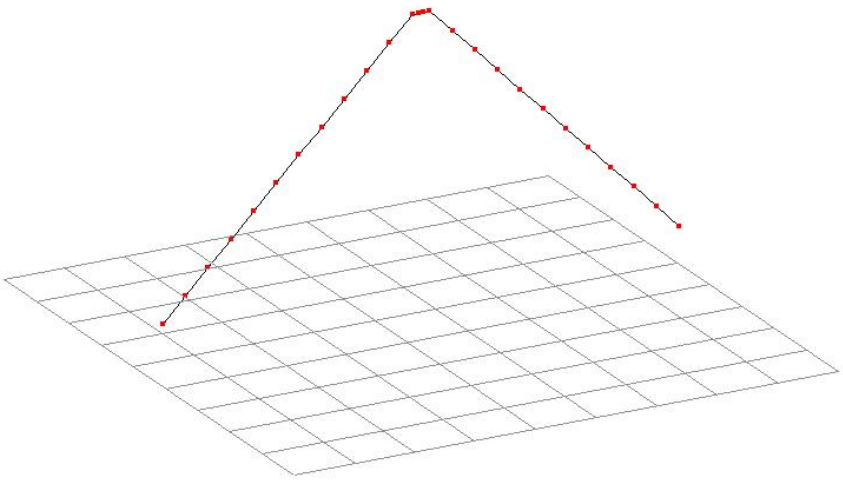

Figure 2: The NEC model used for wire dipoles.

and above, the sidelobe is higher than the mainlobe. Since the difference between the peak and null is less than 3 dB, high beamwidth is maintained in the E-plane at 74 and 80 MHz according the definition given above. However, a deeper null (4 dB relative to the peak) develops at 88 MHz and the beamwidth is reduced, as can be seen in Table 2. An axial ratio of $\leq 3dB$ is achieved at all frequencies < 88 MHz over $|z| \leq 60\,^{\circ}$. For all frequencies, however, the axial ratio increases rapidly above $|z| = 60\,^{\circ}$, and the peak axial ratios reported all occur at $|z| = 74\,^{\circ}$.

As with the sky noise metric, pairing a thin wire inverted-V dipole with a low input impedance leads to very high values of effective collecting area at the zenith near the half-wave resonance point (near 37.5 MHz in this case), and relatively low values at other frequencies. By increasing Z_L, the effective area at higher and lower frequencies can be increased at the expense of the effective area near resonance. For instance, by increasing Z_L from 100 Ω to 400 Ω, the effective area at zenith is increased by a factor of 3.2 at 74 MHz. For each value of Z_L, the transmit and receive-based calculations of effective area exhibit similar characteristics at all frequencies, though the transmit based calculation is up to 4.3 % higher than the receive based calculation.

The thin wire inverted-V dipole is more sensitive to vertically polarized signals at the horizon near the half-wave resonance and less sensitive at other frequencies when a low value of input impedance is used. Sensitivity is increased at higher and lower frequencies by increasing the input impedance.

Table 1: Frequency ranges (in MHz) over which given values of T_{ant} are achieved with thin wire inverted-V dipole for different values of Z_L.

	$T_{ANT} > 500$ K	$T_{ANT} > 1000$ K	$T_{ANT} > 1750$ K	$T_{ANT} > 2500$ K
$Z_L = 100\ \Omega$	26.6 - 56.5	28.9 - 48.5	30.7 - 44.4	31.8 - 42.3
$Z_L = 200\ \Omega$	24.7 - 70.1	27.7 - 55.0	30.2 - 47.9	31.8 - 44.4
$Z_L = 400\ \Omega$	23.3 - 95.8	27.5 - 66.5	31.7 - 53.5	36.1 - 45.6

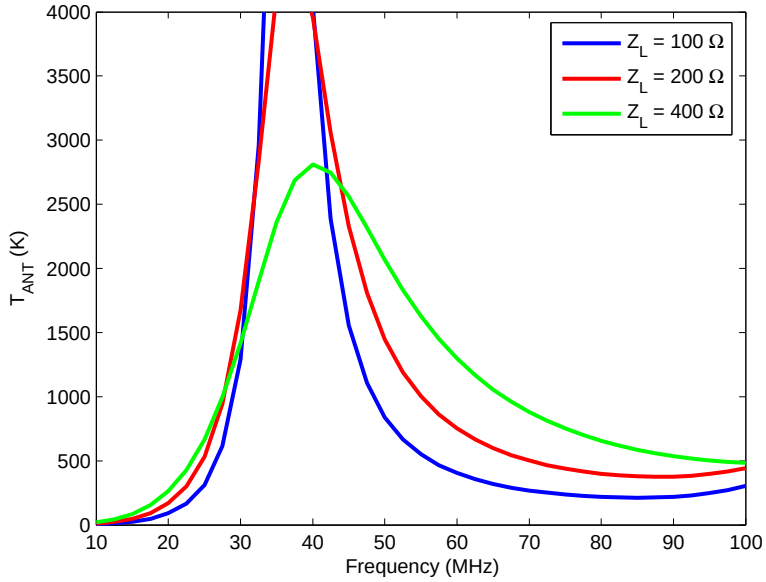

Figure 3: Sky noise frequency response of thin wire inverted-V dipole for different values of Z_L.

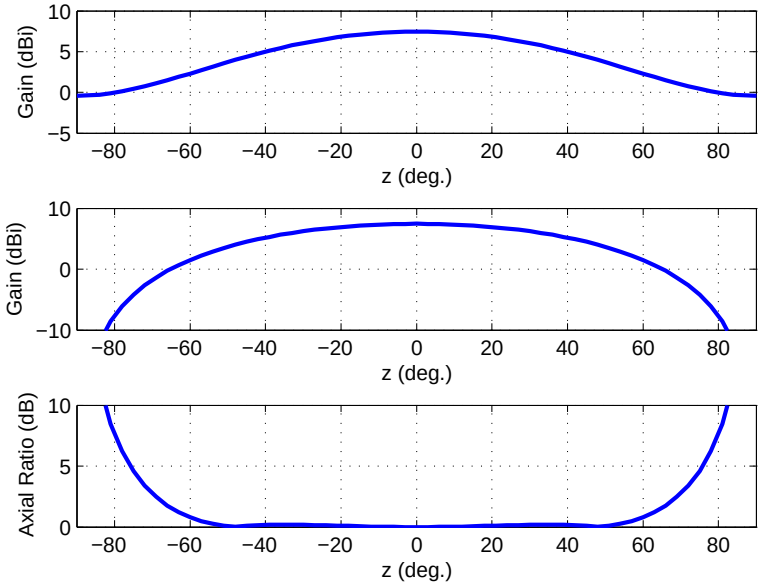

Figure 4: Co-polarized radiation patterns in E-plane (top) and H-plane (middle), and axial ratio (bottom) of thin wire inverted-V dipole at 10.0 MHz.

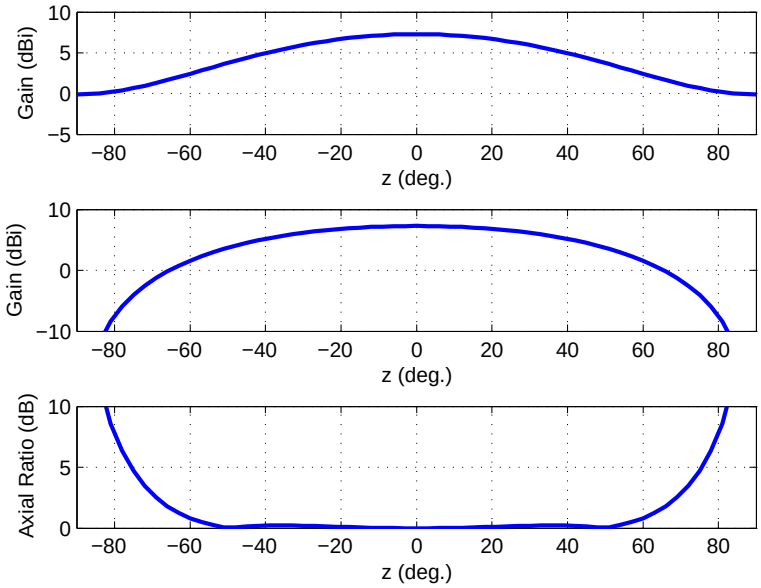

Figure 5: Co-polarized radiation patterns in E-plane (top) and H-plane (middle), and axial ratio (bottom) of thin wire inverted-V dipole at 20.0 MHz.

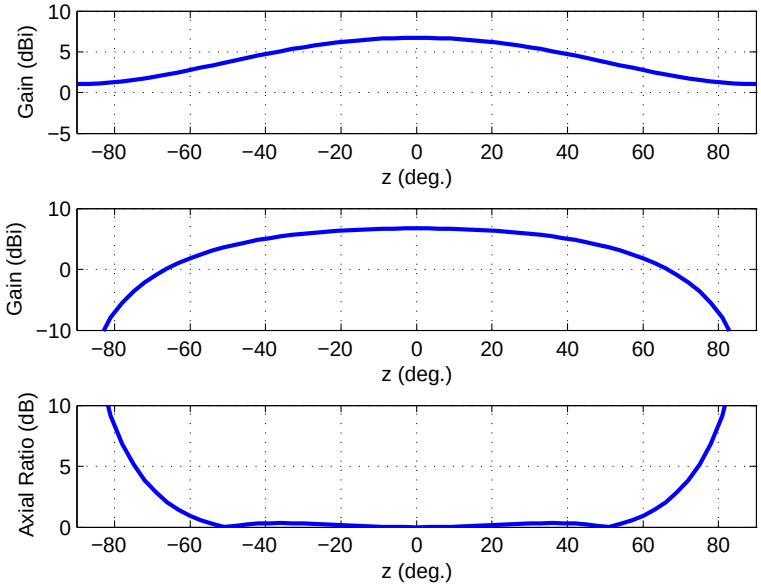

Figure 6: Co-polarized radiation patterns in E-plane (top) and H-plane (middle), and axial ratio (bottom) of thin wire inverted-V dipole at 38.0 MHz.

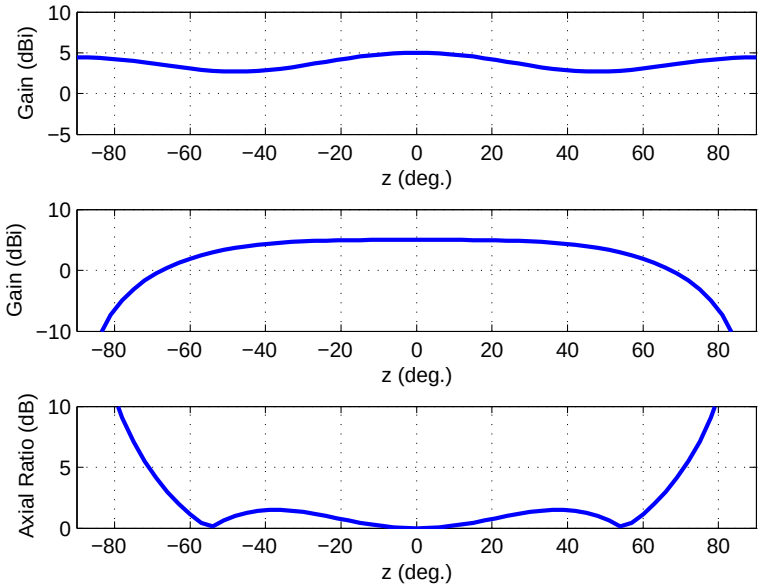

Figure 7: Co-polarized radiation patterns in E-plane (top) and H-plane (middle), and axial ratio (bottom) of thin wire inverted-V dipole at 74.0 MHz.

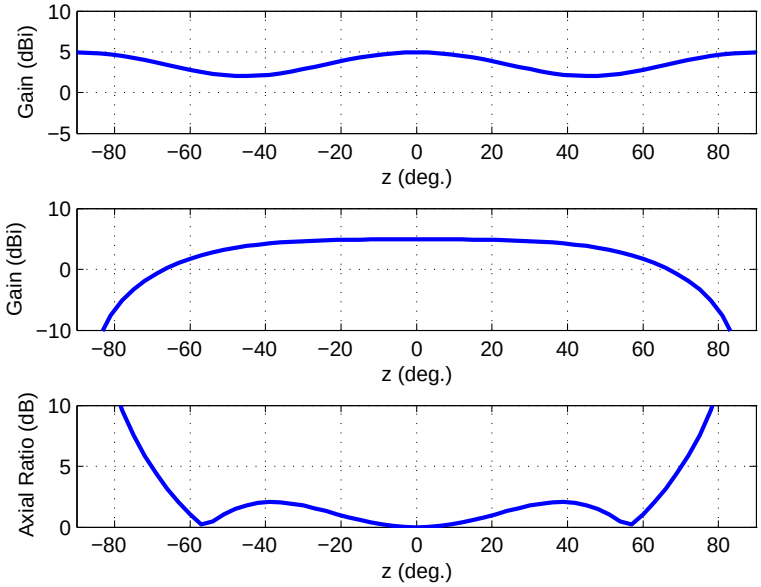

Figure 8: Co-polarized radiation patterns in E-plane (top) and H-plane (middle), and axial ratio (bottom) of thin wire inverted-V dipole at 80.0 MHz.

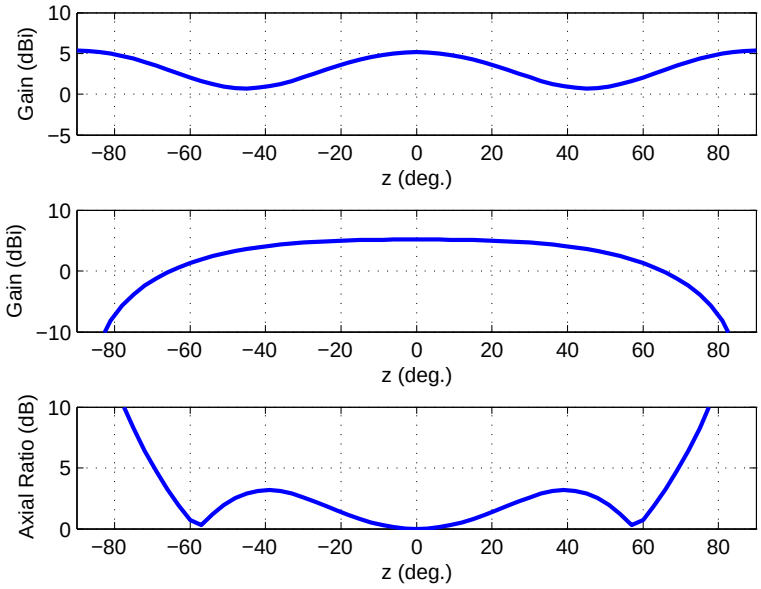

Figure 9: Co-polarized radiation patterns in E-plane (top) and H-plane (middle), and axial ratio (bottom) of thin wire inverted-V dipole at 88.0 MHz.

Table 2: Half-power beamwidth in principal planes at different frequencies for thin wire inverted-V dipole.

Freq (MHz)	E-plane HPBW (deg)	H-plane HPBW (deg)
10.0	88.9	90.5
20.0	91.3	92.7
38.0	100.6	100.5
74.0	180.0	119.2
80.0	180.0	118.0
88.0	58.8	111.3

Table 3: Maximum axial ratio for $z \leq 74^\circ$ for thin wire inverted-V dipole.

Freq (MHz)	max. AR (dB)
10.0	4.6
20.0	4.7
38.0	5.2
74.0	7.1
80.0	7.6
88.0	8.3

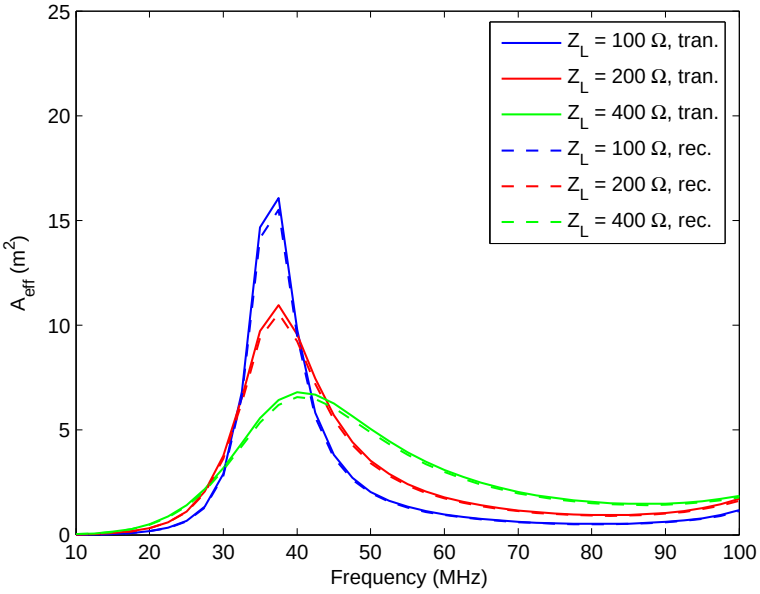

Figure 10: Effective collecting area frequency response at boresight of thin wire inverted-V dipole for different values of Z_L.

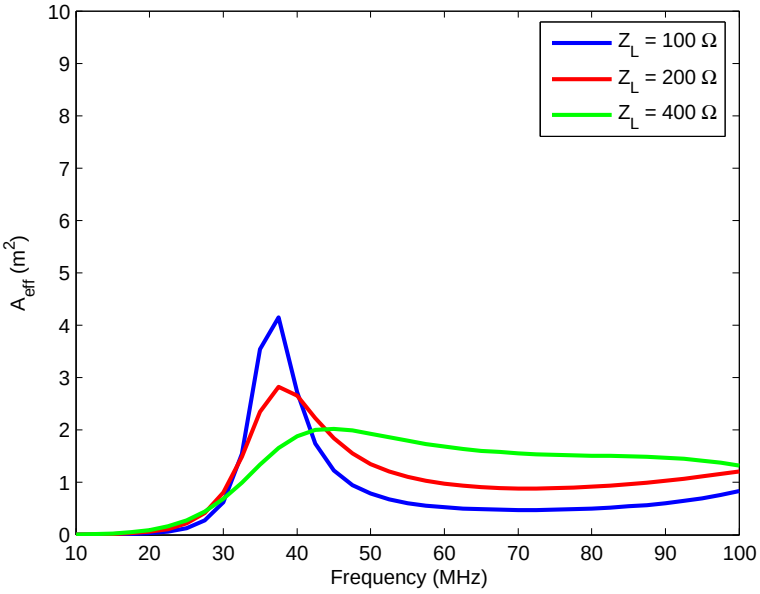

Figure 11: Effective collecting area frequency response at horizon of thin wire inverted-V dipole for different values of Z_L.

4 Thick Wire Inverted-V Dipole

As it is expected that the bandwidth of the inverted-V dipole would increase by increasing the radius of the wire elements, all of the performance metrics were re-calculated assuming the radius of the wire element was increased to 10.0 mm. This wire radius is intended to simulate a thick wire braid as used in the fork dipole (see section 7). All other dimensions of the antenna were assumed to be the same as in section 3.

The calculated metrics for the thick wire dipole are provided in Figures 12-20 and Tables 4-6 in the remainder of this section.

Similar trends with frequency and input impedance are seen in each of the performance metrics for the thick wire inverted-V as those for the thin wire version. Noted differences between the results for the two antennas are summarized below:

- As expected, the sky noise bandwidth of the thick wire inverted-V is higher than that of the thin wire version. For $Z_L = 100\ \Omega$, the bandwidth is increased from 19.6 MHz wide for the thin wire dipole to 26.2 MHz wide for the thick wire dipole. For $Z_L = 400\ \Omega$, the bandwidth is increased from 39 MHz wide to 48.6 MHz wide.
- The height of sidelobes and depths of nulls (up to 5 dB relative to the peak at 88 MHz) are greater for the thick wire dipole than the thin wire dipole. This causes the calculated beamwidths to be somewhat lower for the thick wire dipole.
- The maximum axial ratio values are slightly higher at all frequencies for the thick wire dipole.
- The thick wire dipole exhibits somewhat higher values of effective area at the zenith for all frequencies and all values of input impedance. Interestingly, the receive-based calculation of effective area is higher (up to 9.2 %) than the transmit calculation for the thick wire dipole; the opposite was true for the thin wire dipole.
- Sensitivity to vertically polarized signals at the horizon is also higher at all frequencies and values of input impedance for the thick wire dipole than the thin wire dipole.

Table 4: Frequency ranges (in MHz) over which given values of T_{ant} are achieved with thick wire inverted-V dipole for different values of Z_L.

	$T_{ANT} > 500$ K	$T_{ANT} > 1000$ K	$T_{ANT} > 1750$ K	$T_{ANT} > 2500$ K
$Z_L = 100\ \Omega$	23.7 - 65.4	26.3 - 52.5	28.4 - 46.6	29.8 - 43.8
$Z_L = 200\ \Omega$	21.8 -100.0	25.1 - 62.7	27.8 - 52.4	29.7 - 47.4
$Z_L = 400\ \Omega$	20.8 - 95.9	25.3 - 73.9	29.9 - 61.3	33.9 - 53.5

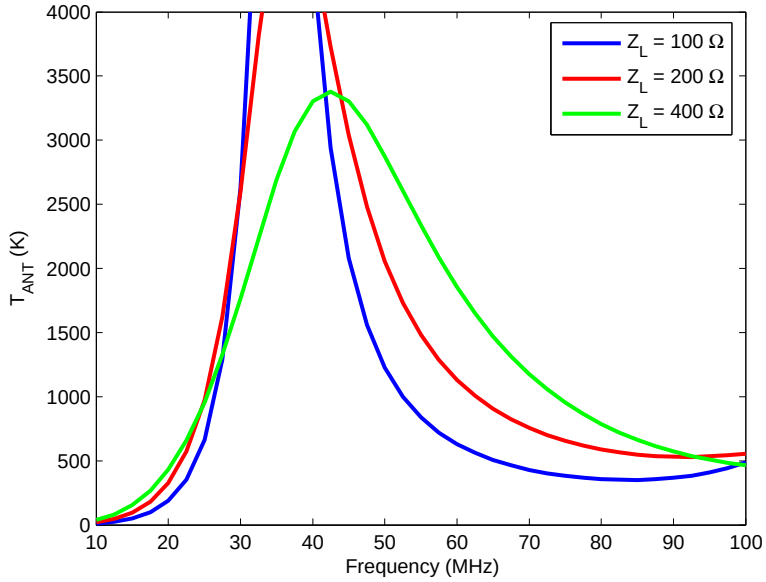

Figure 12: Sky noise frequency response of thick wire inverted-V dipole for different values of Z_L.

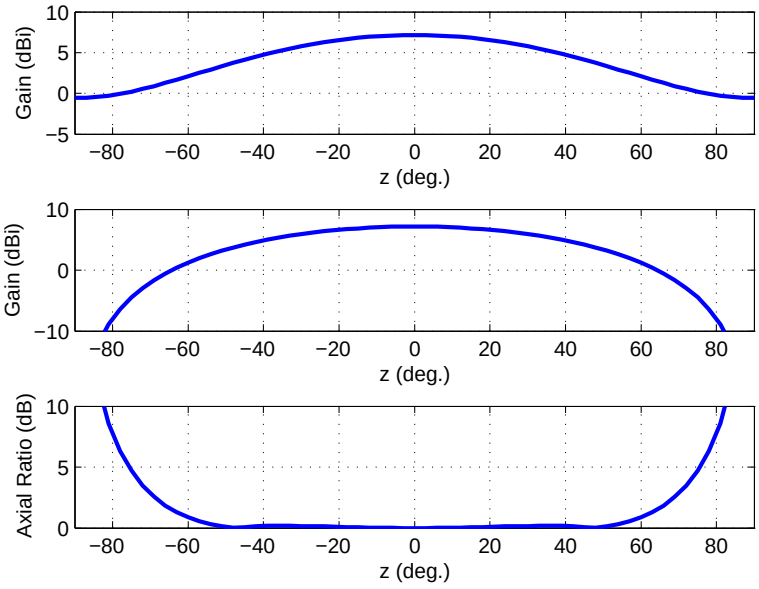

Figure 13: Co-polarized radiation patterns in E-plane (top) and H-plane (middle), and axial ratio (bottom) of thick wire inverted-V dipole at 10.0 MHz.

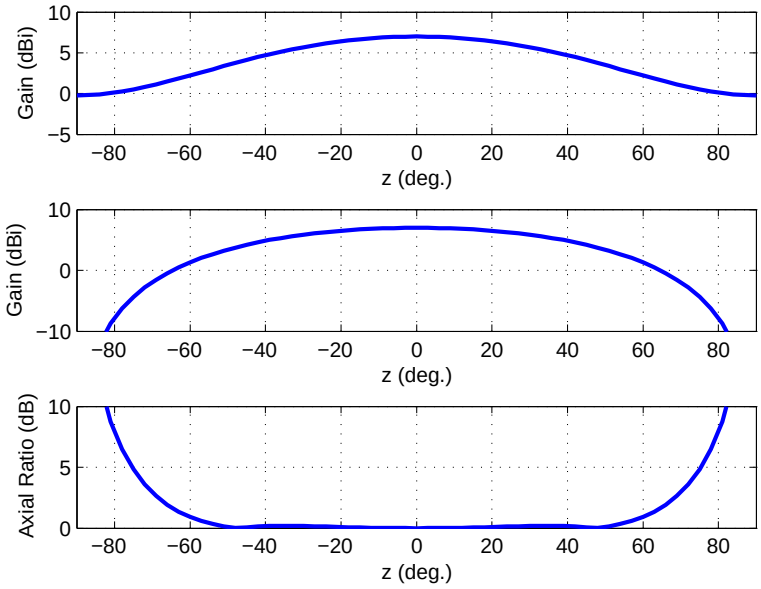

Figure 14: Co-polarized radiation patterns in E-plane (top) and H-plane (middle), and axial ratio (bottom) of thick wire inverted-V dipole at 20.0 MHz.

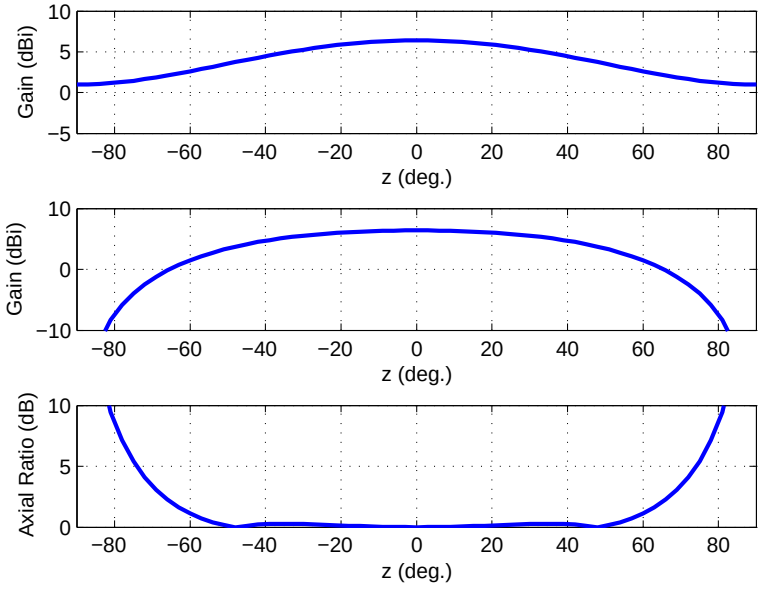

Figure 15: Co-polarized radiation patterns in E-plane (top) and H-plane (middle), and axial ratio (bottom) of thick wire inverted-V dipole at 38.0 MHz.

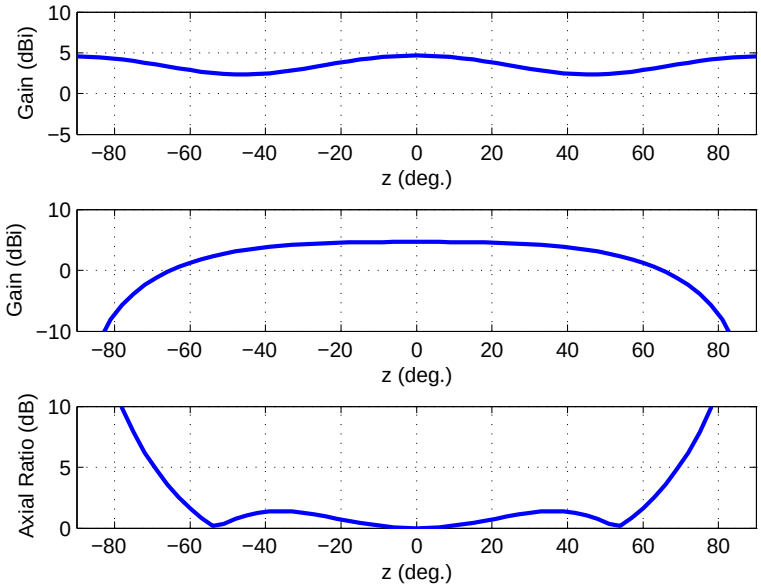

Figure 16: Co-polarized radiation patterns in E-plane (top) and H-plane (middle), and axial ratio (bottom) of thick wire inverted-V dipole at 74.0 MHz.

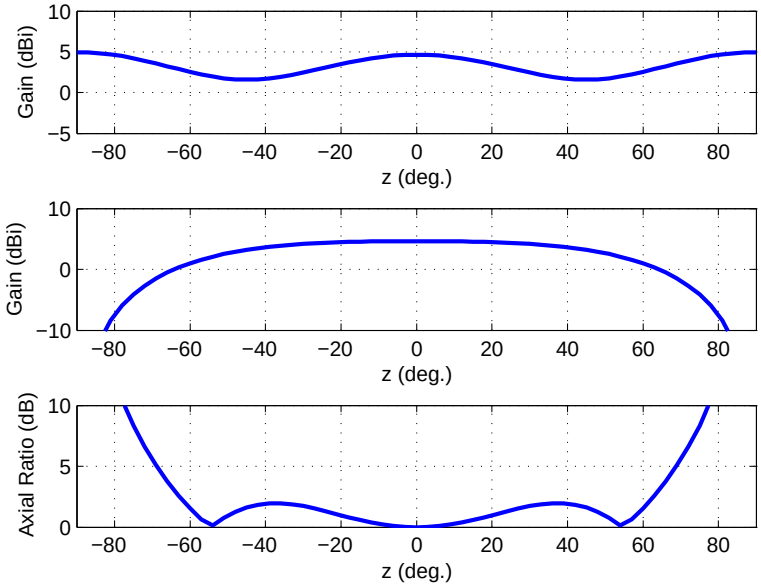

Figure 17: Co-polarized radiation patterns in E-plane (top) and H-plane (middle), and axial ratio (bottom) of thick wire inverted-V dipole at 80.0 MHz.

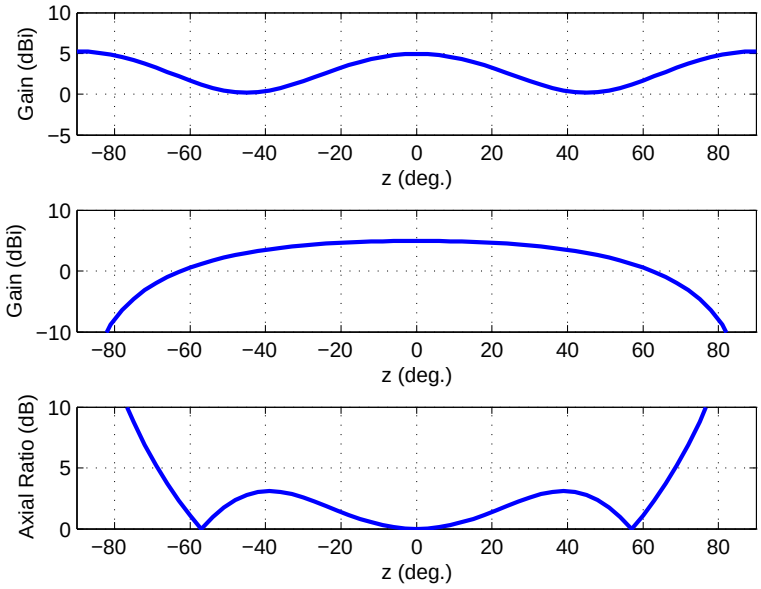

Figure 18: Co-polarized radiation patterns in E-plane (top) and H-plane (middle), and axial ratio (bottom) of thick wire inverted-V dipole at 88.0 MHz.

Table 5: Half-power beamwidth in principal planes at different frequencies for thick wire inverted-V dipole.

Freq (MHz)	E-plane HPBW (deg)	H-plane HPBW (deg)
10.0	89.5	90.6
20.0	91.9	92.6
38.0	103.0	100.3
74.0	180.0	115.6
80.0	83.0	113.4
88.0	56.0	105.2

Table 6: Maximum axial ratio for $z \leq 74^\circ$ for thick wire inverted-V dipole.

Freq (MHz)	max. AR (dB)
10.0	4.7
20.0	4.8
38.0	5.4
74.0	7.9
80.0	8.3
88.0	8.8

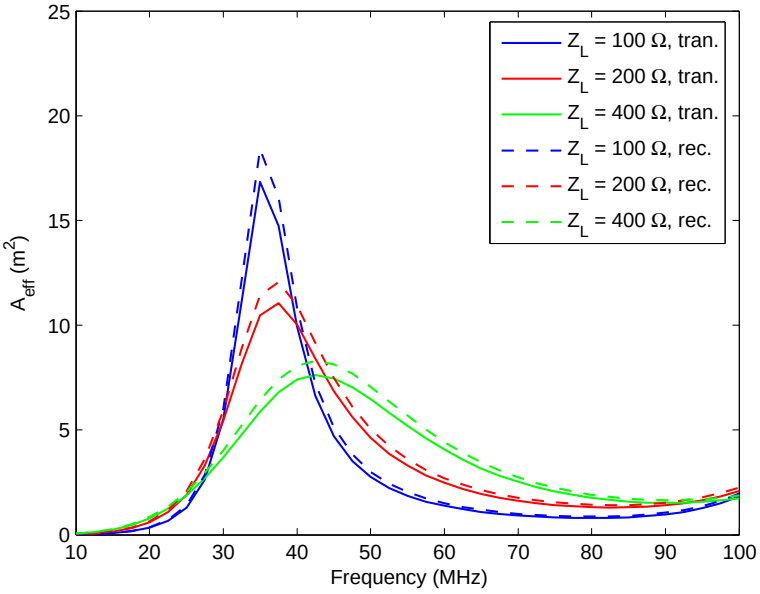

Figure 19: Effective collecting area frequency response at boresight of thick wire inverted-V dipole for different values of Z_L.

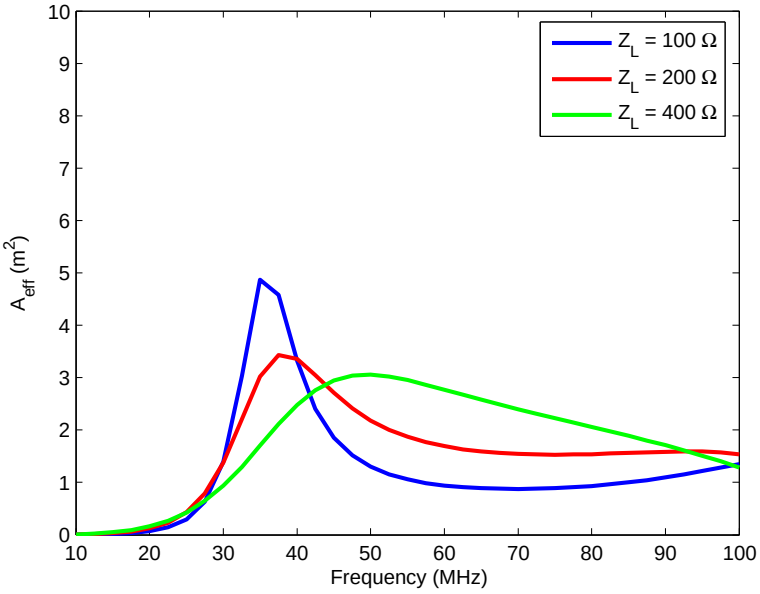

Figure 20: Effective collecting area frequency response at horizon of thick wire inverted-V dipole for different values of Z_L.

5 MWA-like Dipole

The antenna element design for the MWA LFD array is shown in Figure 21. It consists of a crossed pair of vertically oriented bow-tie dipoles. Design information for this antenna was provided by Brian Corey of Haystack Observatory. As this antenna operates nominally between 80 to 300 MHz, it is necessary to scale up its dimensions in order to compare it with antennas designed for use at LWA frequencies. A common scaling factor of 3.6 was applied to all of the dimensions of the MWA dipole, which provides a good fit to the LWA frequency range. The conductors of the scaled MWA dipole were assumed to be thick wires with a radius of 10 mm. This wire radius is intended to simulate a thick wire braid as used in the fork dipole (see section 7).

The NEC model used to simulate the scaled MWA dipole is shown in Figure 22. The calculated metrics for the scaled MWA dipole are provided in Figures 23-31 and Tables 7-9 in the remainder of this section.

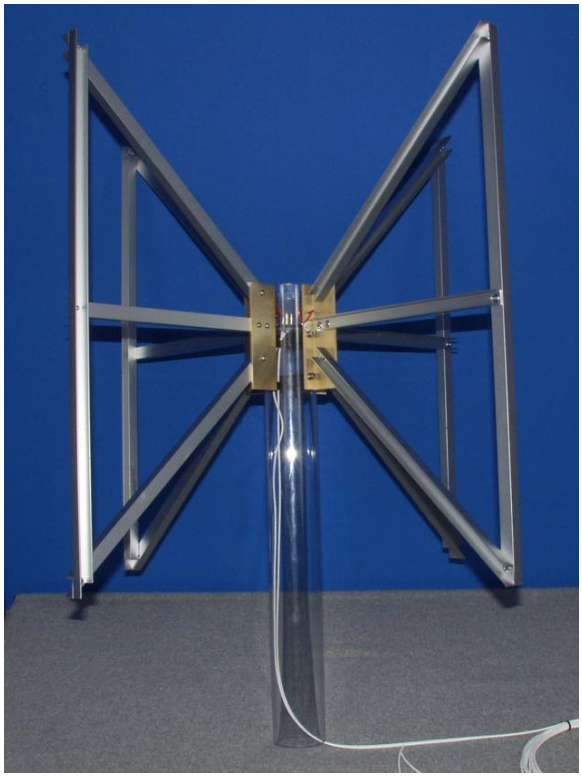

Figure 21: The MWA LFD antenna [4].

Unlike the wire dipoles considered above, the MWA dipole provides wide sky noise bandwidth with lower values of Z_L. For instance, $T_{ANT} \geq 1000$ K is achieved over 20.4 to 72.6 MHz with $Z_L = 100\ \Omega$. By increasing Z_L to 200 Ω, which appears to provide the best trade-off for all values of Z_L considered, $T_{ANT} \geq 1000$ K is achieved over 19.8 to 84.6 MHz, which covers the entire LWA band. A "bump" is noted in the sky noise response at roughly 95 MHz, which may be due to a unexpected mode being set up in the antenna.

Nulls are exhibited at the horizon in both the E- and H-planes patterns of the MWA dipole, which is unlike the wire dipoles. However, unlike the nulls in the H-plane which truly go to zero, the E-plane nulls of the MWA dipole are only 10 to 25 dB down from the pattern peaks. The E-plane nulls occur since the arms of the MWA dipole are not bent downward like the other dipole

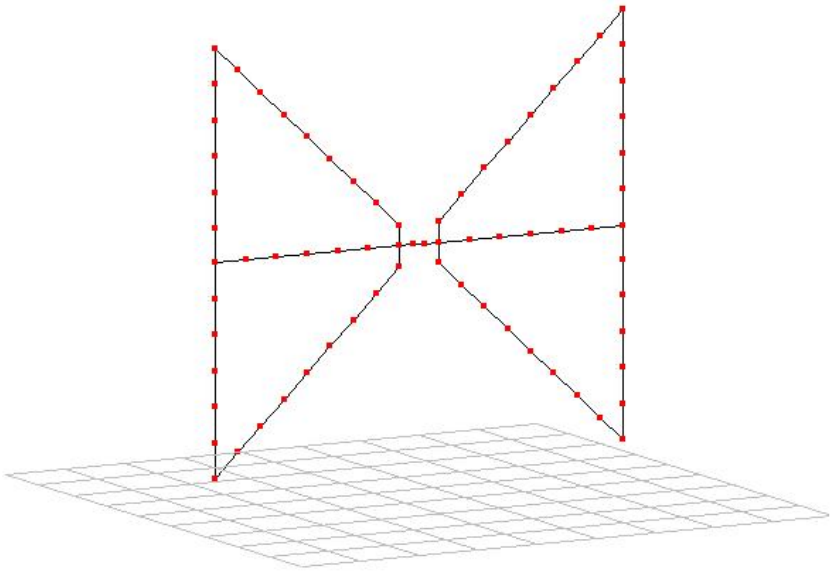

Figure 22: The NEC model used for the MWA-like dipole.

design considered in this report. This aspect of the MWA dipole causes a number of undesirable characteristics in its radiation patterns:

- Very low HPBW values are exhibited in E-plane patterns at lower frequencies.
- The pattern shapes in the two principal planes are not well "matched". This leads to very high maximum axial ratio values, for example 23.9 dB at 74 MHz. Even for $|z| \leq 60\,^{\circ}$, the axial ratio is > 5 dB for all frequencies ≤ 38 MHz and > 9 dB for all frequencies ≥ 74 MHz.
- For frequencies ≥ 74 MHz, nulls appear in the patterns at the zenith. Above 74 MHz, nulls are more than 3 dB down from the peak which reduces the pattern beamwidth according to the definition used in this report.

High values of effective collecting area are achieved at the zenith over a wide frequency range for each value of Z_L. $Z_L = 200\ \Omega$ provides the best trade-off between high values of collecting area and bandwidth. As with the thick wire dipole, the receive based calculation of collecting area is greater than the transmit based calculation. Below 90 MHz, the typical difference between the two calculations is between 6.5 to 8.0 %. However large differences, between 15 to 91 %, are noted between 90 to 100 MHz. This behavior is likely to be related to the "bump" noted earlier in the sky noise frequency response.

As compared with other dipole designs considered in this report, the MWA dipole exhibits very low sensitivity to vertically polarized signals at the horizon over most frequencies. This is due to the nulls at the horizon, which are evident in the E-plane patterns of the MWA dipole.

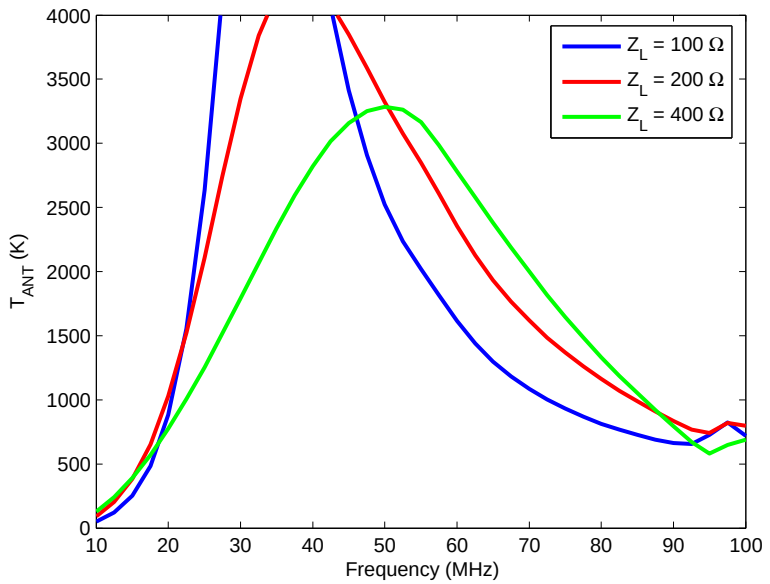

Figure 23: Sky noise frequency response of MWA-like dipole for different values of Z_L.

Table 7: Frequency ranges (in MHz) over which given values of T_{ant} are achieved with MWA-like dipole for different values of Z_L.

	$T_{ANT} > 500$ K	$T_{ANT} > 1000$ K	$T_{ANT} > 1750$ K	$T_{ANT} > 2500$ K
$Z_L = 100\ \Omega$	17.6 -100.0	20.4 - 72.6	22.9 - 58.3	24.7 - 50.2
$Z_L = 200\ \Omega$	16.1 -100.0	19.8 - 84.6	23.5 - 67.8	26.5 - 58.6
$Z_L = 400\ \Omega$	16.5 -100.0	22.4 - 86.0	29.6 - 73.5	36.6 - 63.5

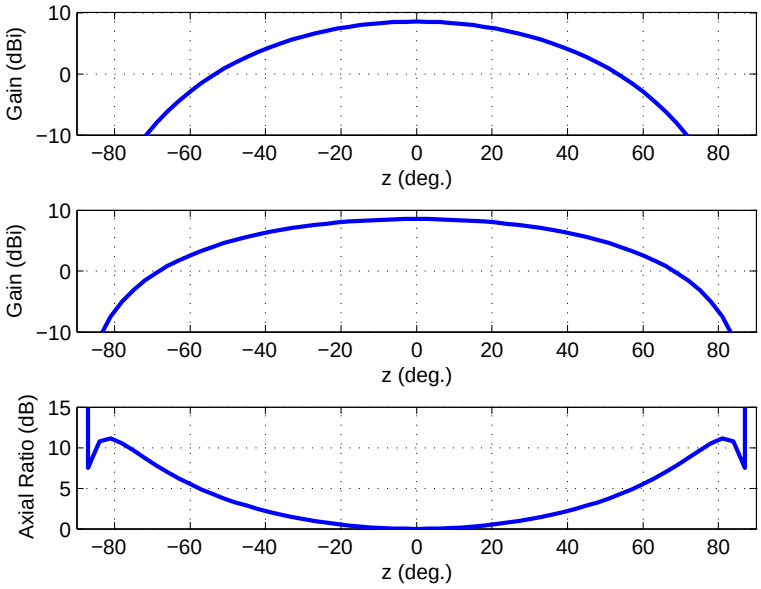

Figure 24: Co-polarized radiation patterns in E-plane (top) and H-plane (middle), and axial ratio (bottom) of MWA-like dipole at 10.0 MHz.

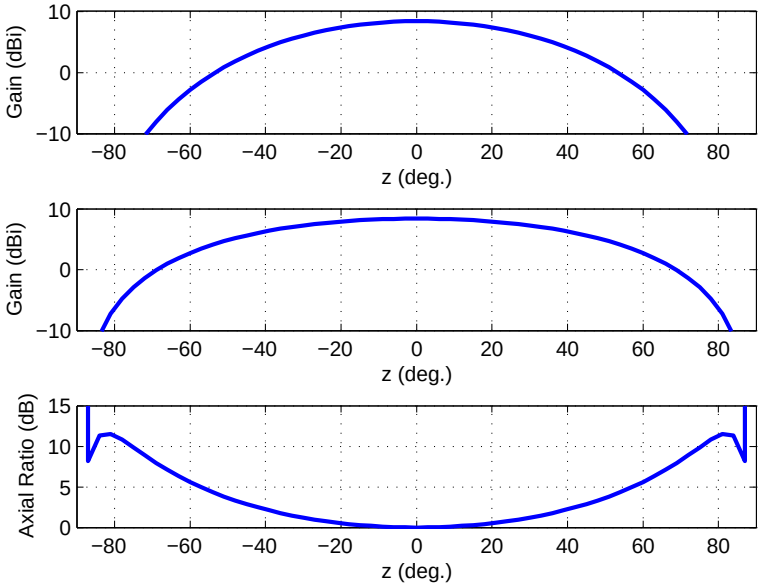

Figure 25: Co-polarized radiation patterns in E-plane (top) and H-plane (middle), and axial ratio (bottom) of MWA-like dipole at 20.0 MHz.

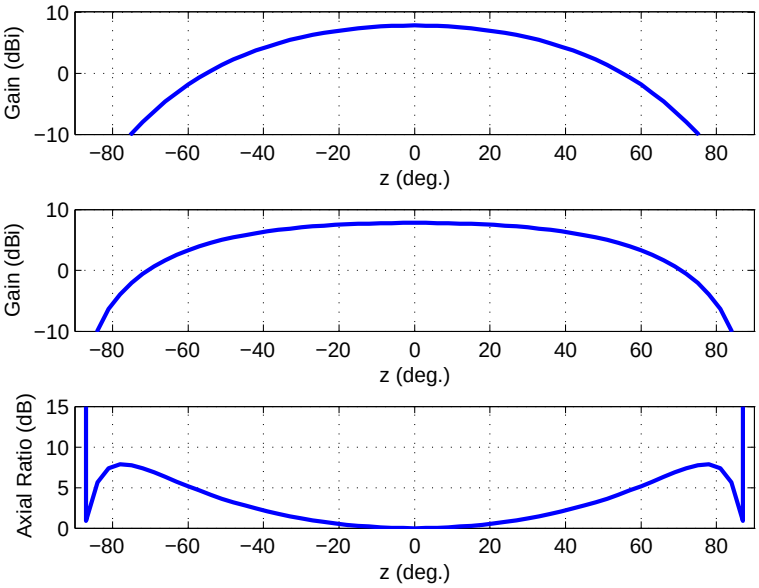

Figure 26: Co-polarized radiation patterns in E-plane (top) and H-plane (middle), and axial ratio (bottom) of MWA-like dipole at 38.0 MHz.

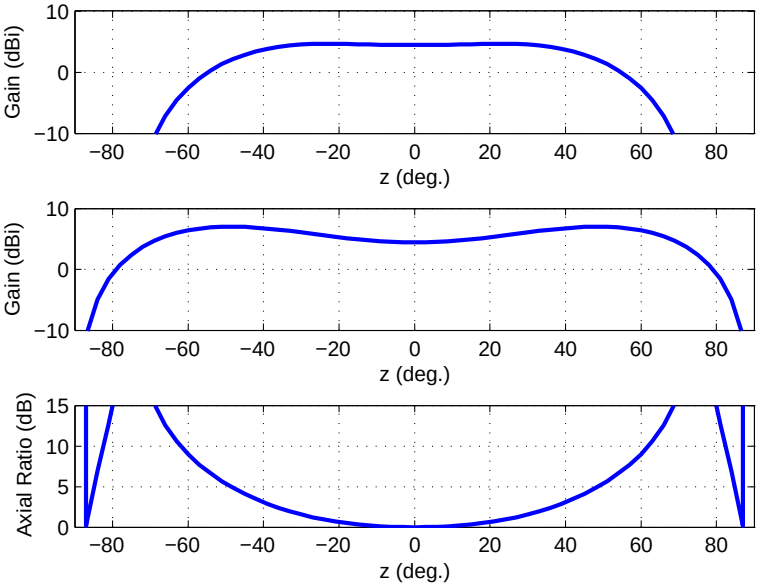

Figure 27: Co-polarized radiation patterns in E-plane (top) and H-plane (middle), and axial ratio (bottom) of MWA-like dipole at 74.0 MHz.

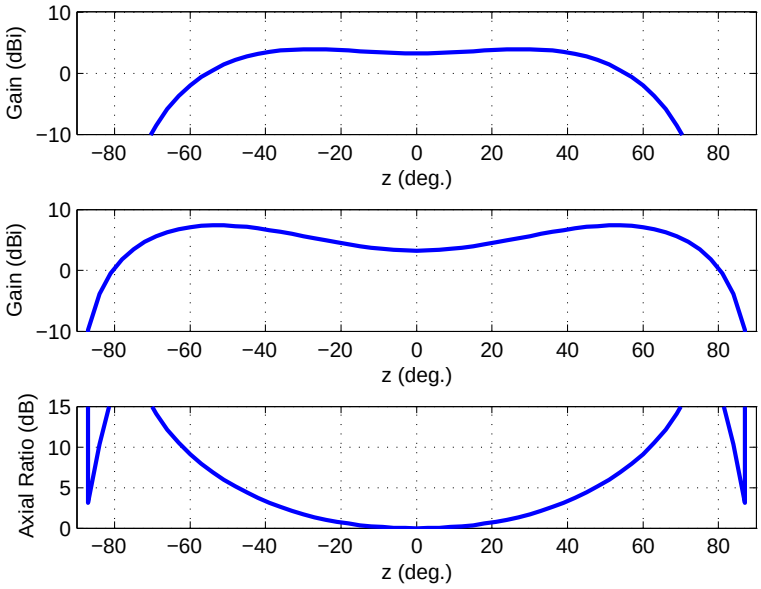

Figure 28: Co-polarized radiation patterns in E-plane (top) and H-plane (middle), and axial ratio (bottom) of MWA-like dipole at 80.0 MHz.

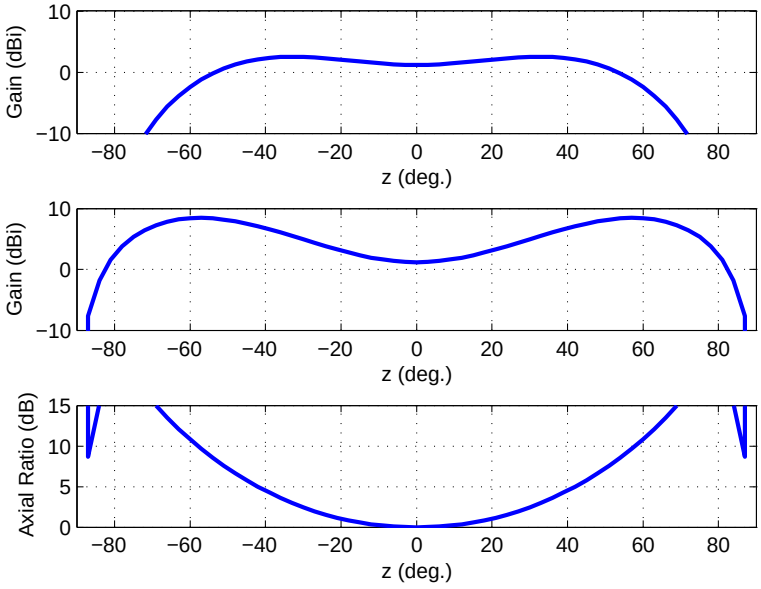

Figure 29: Co-polarized radiation patterns in E-plane (top) and H-plane (middle), and axial ratio (bottom) of MWA-like dipole at 88.0 MHz.

Table 8: Half-power beamwidth in principal planes at different frequencies for MWA-like dipole.

Freq (MHz)	E-plane HPBW (deg)	H-plane HPBW (deg)
10.0	66.5	90.5
20.0	67.5	93.1
38.0	73.3	104.4
74.0	101.2	153.4
80.0	109.2	70.9
88.0	117.0	52.2

Table 9: Maximum axial ratio for z $\leq 74^\circ$ for MWA-like dipole.

Freq (MHz)	max. AR (dB)
10.0	9.6
20.0	9.9
38.0	7.8
74.0	23.9
80.0	19.3
88.0	18.5

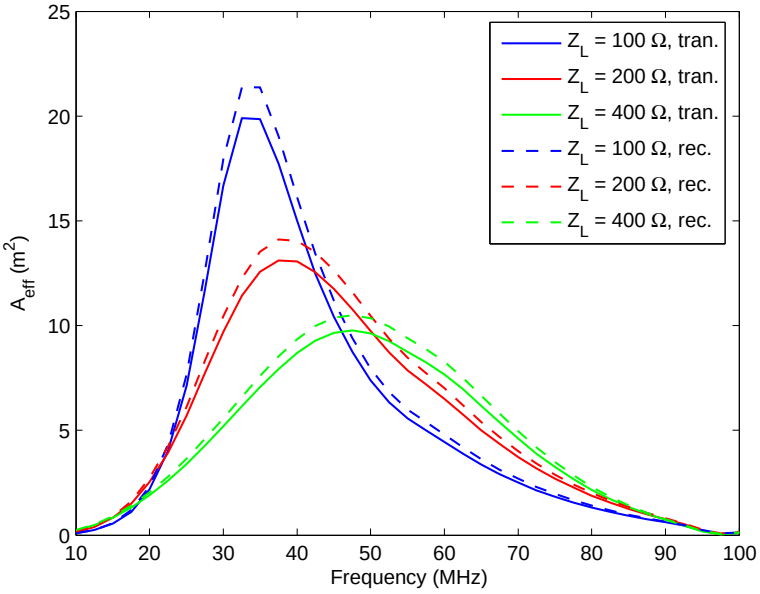

Figure 30: Effective collecting area frequency response at boresight of MWA-like dipole for different values of Z_L.

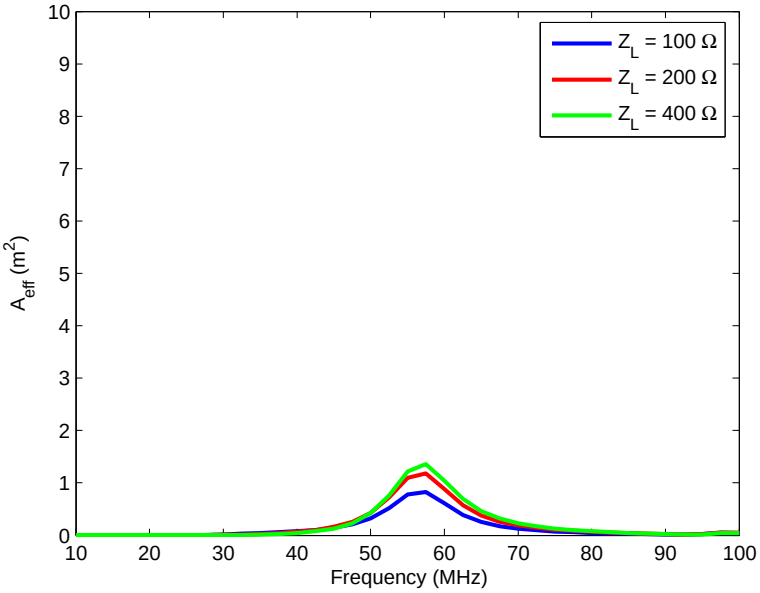

Figure 31: Effective collecting area frequency response at horizon of MWA-like dipole for different values of Z_L.

6 Blade Dipole

The "big blade" dipole, which is a candidate antenna element design for LWA, is shown in Figure 32. The dimensions assumed are L_b (length of element) = 1.72 m, L_{tap} (length of tapered section of element) = 0.35 m, β (taper angle of element) = 30 °, W_b (width of element) = 0.42 m, α (droop angle) = 45 °, H (height of antenna above ground)= 1.52 m, and w_f (feed width) = 0.10 m.

The NEC model used to simulate the big blade dipole is shown in Figure 33. The wire radius used in this model was chosen according to $r_w = d_{mesh}/(2\pi)$ where d_{mesh} is the grid spacing used in the model. The calculated metrics for the big blade dipole are provided in Figures 34-42 and Tables 10-12 in the remainder of this section.

Figure 32: The big blade antenna. Photo obtained from [5].

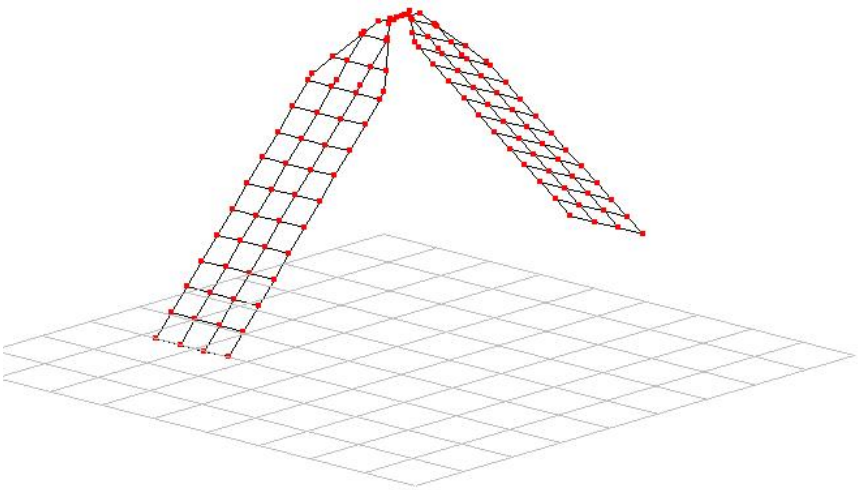

Figure 33: The NEC model used for the blade dipole.

Like the MWA dipole, the blade dipole achieves wide sky noise bandwidth with lower values of Z_L. For $Z_L = 200\ \Omega$, which appears to offer the best performance, $T_{ANT} \geq 1000$ K is achieved over 20.3 to 75.6 MHz. This covers most of the LWA operating band, but is a slightly narrower bandwidth than offered by the MWA dipole for the same value of T_{ANT}.

The blade dipole patterns exhibit all the same characteristics and trends with frequency that the wire inverted-V dipoles do. The radiation patterns are sidelobe free for frequencies ≤ 38 MHz, but develop sidelobes at 74 MHz and higher frequencies. For frequencies ≥ 80 MHz, the nulls are $>$ 3 dB down from the pattern peak, which causes a reduction in the calculated beamwidth. The HPBW values for the blade dipole are similar to those of the thick wire inverted-V dipole at all frequencies. The axial ratio values of the blade and thick wire inverted-V dipoles are also similar at all frequencies.

As with the MWA dipole, high values of effective collecting area are achieved at the zenith over a wide frequency range with $Z_L = 200\ \Omega$ giving the best performance. Unlike the thick wire inverted-V dipole and MWA dipoles, the transmit based calculation of effective area is higher than the receive based calculation by up to 16.8 %.

The blade exhibits relatively high sensitivity to vertically polarized signals incident from the horizon over a wide frequency range for each of the values of Z_L considered.

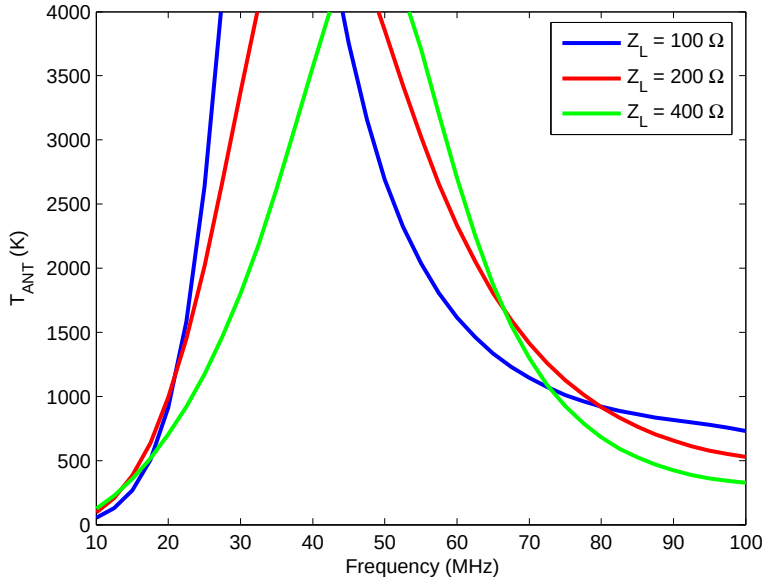

Figure 34: Sky noise frequency response of blade dipole for different values of Z_L.

Table 10: Frequency ranges (in MHz) over which given values of T_{ant} are achieved with blade dipole for different values of Z_L.

	$T_{ANT} > 500$ K	$T_{ANT} > 1000$ K	$T_{ANT} > 1750$ K	$T_{ANT} > 2500$ K
$Z_L = 100\ \Omega$	17.4 -100.0	20.3 - 75.6	22.9 - 58.2	24.7 - 51.3
$Z_L = 200\ \Omega$	16.2 -100.0	20.0 - 77.9	23.8 - 65.7	26.8 - 58.7
$Z_L = 400\ \Omega$	17.2 - 86.1	23.3 - 73.8	29.6 - 66.0	34.3 - 61.1

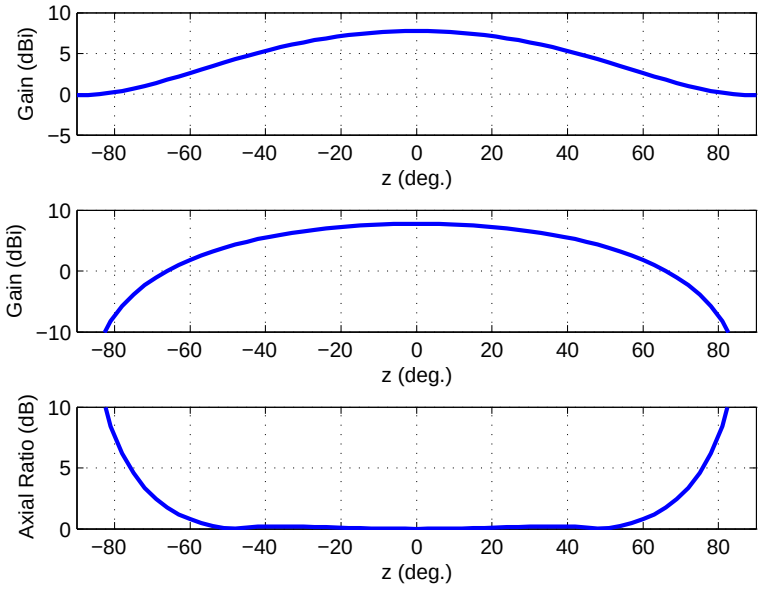

Figure 35: Co-polarized radiation patterns in E-plane (top) and H-plane (middle), and axial ratio (bottom) of blade dipole at 10.0 MHz.

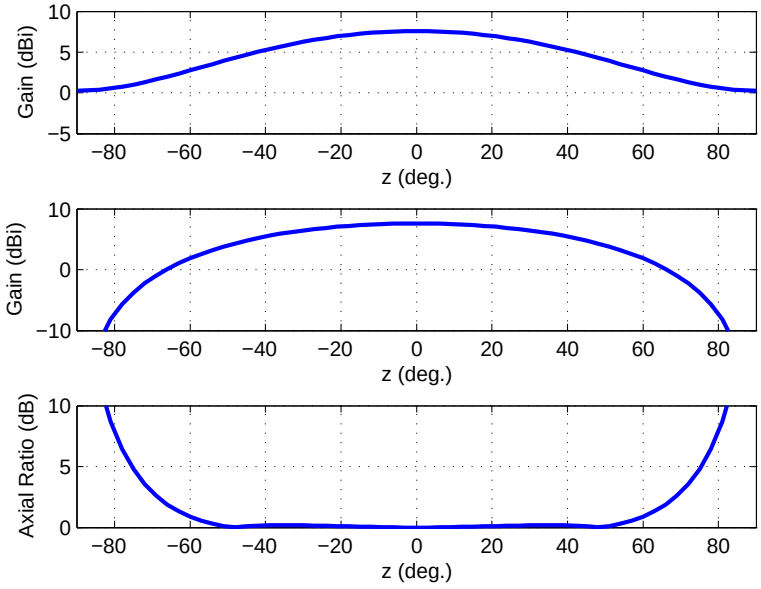

Figure 36: Co-polarized radiation patterns in E-plane (top) and H-plane (middle), and axial ratio (bottom) of blade dipole at 20.0 MHz.

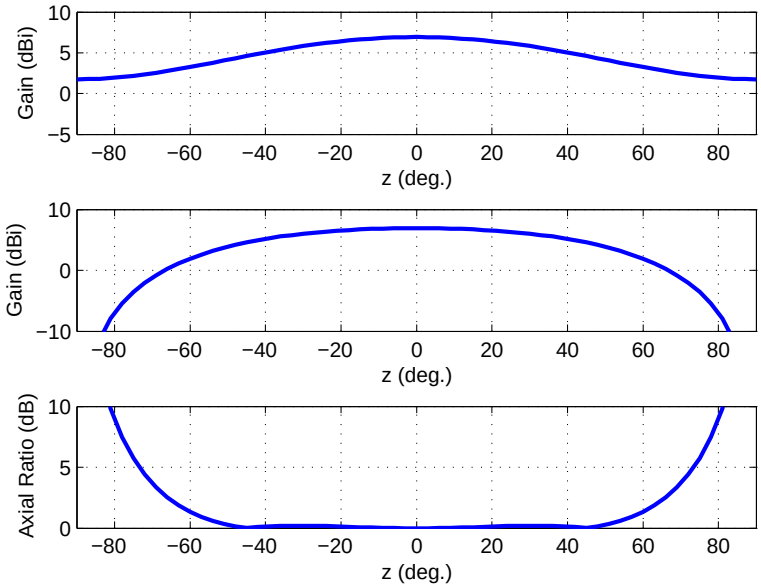

Figure 37: Co-polarized radiation patterns in E-plane (top) and H-plane (middle), and axial ratio (bottom) of blade dipole at 38.0 MHz.

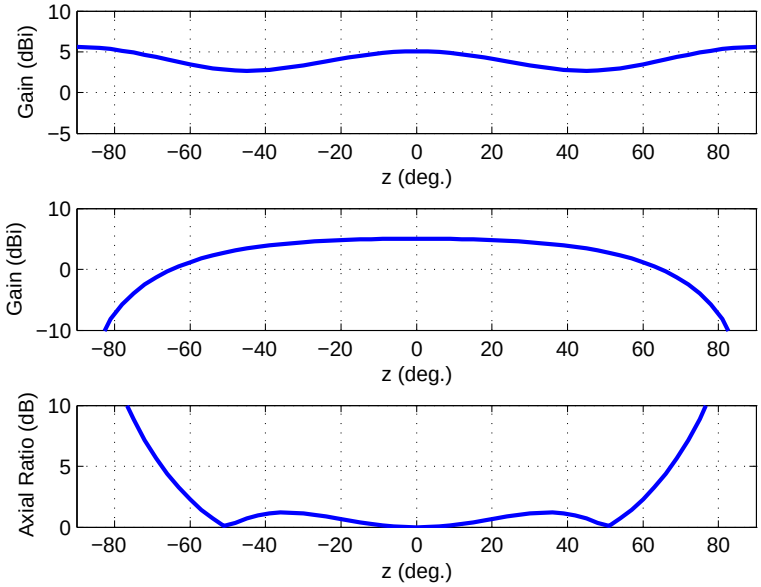

Figure 38: Co-polarized radiation patterns in E-plane (top) and H-plane (middle), and axial ratio (bottom) of blade dipole at 74.0 MHz.

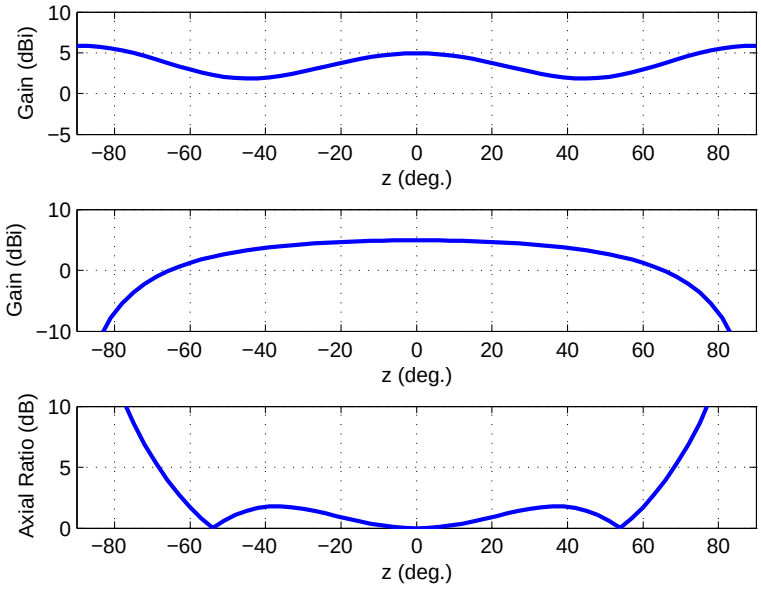

Figure 39: Co-polarized radiation patterns in E-plane (top) and H-plane (middle), and axial ratio (bottom) of blade dipole at 80.0 MHz.

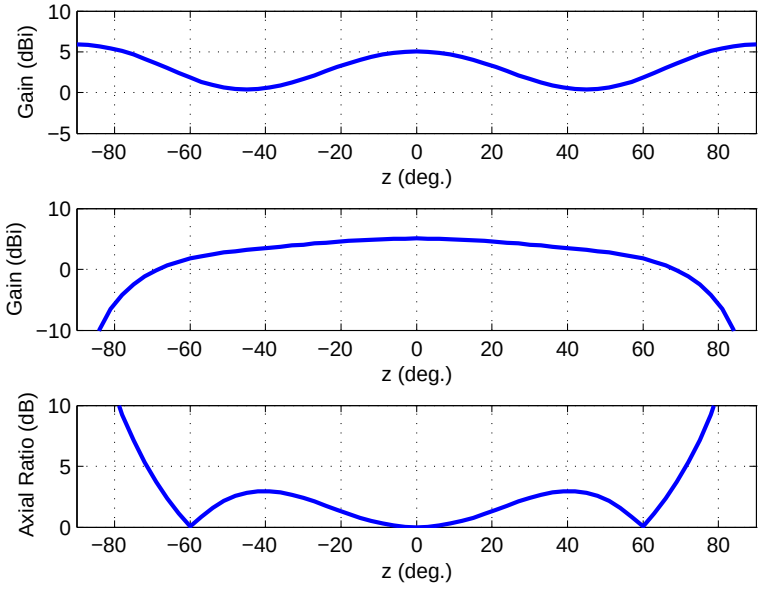

Figure 40: Co-polarized radiation patterns in E-plane (top) and H-plane (middle), and axial ratio (bottom) of blade dipole at 88.0 MHz.

Table 11: Half-power beamwidth in principal planes at different frequencies for blade dipole.

Freq (MHz)	E-plane HPBW (deg)	H-plane HPBW (deg)
10.0	88.7	90.5
20.0	91.5	92.5
38.0	104.9	99.3
74.0	180.0	110.7
80.0	79.6	111.9
88.0	54.8	115.6

Table 12: Maximum axial ratio for z $\leq 74^\circ$ for blade dipole.

Freq (MHz)	max. AR (dB)
10.0	4.6
20.0	4.8
38.0	5.7
74.0	8.8
80.0	8.6
88.0	7.1

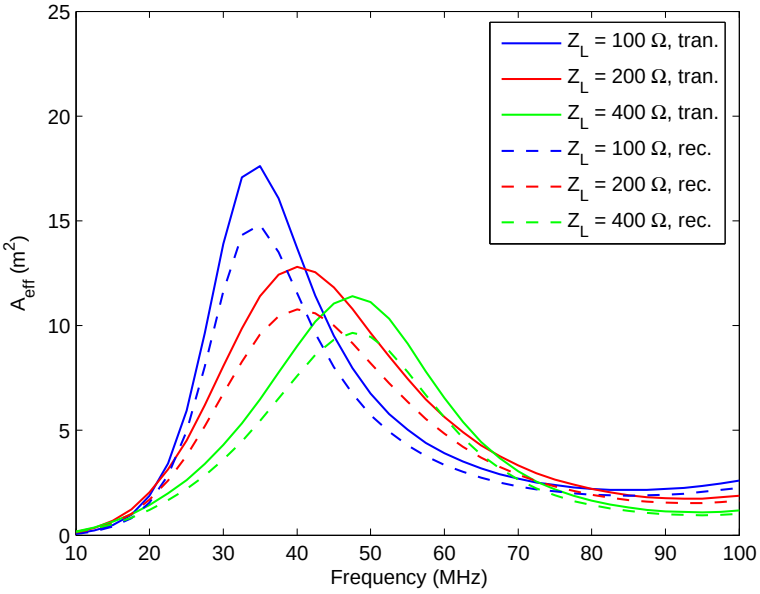

Figure 41: Effective collecting area frequency response at boresight of blade dipole for different values of Z_L.

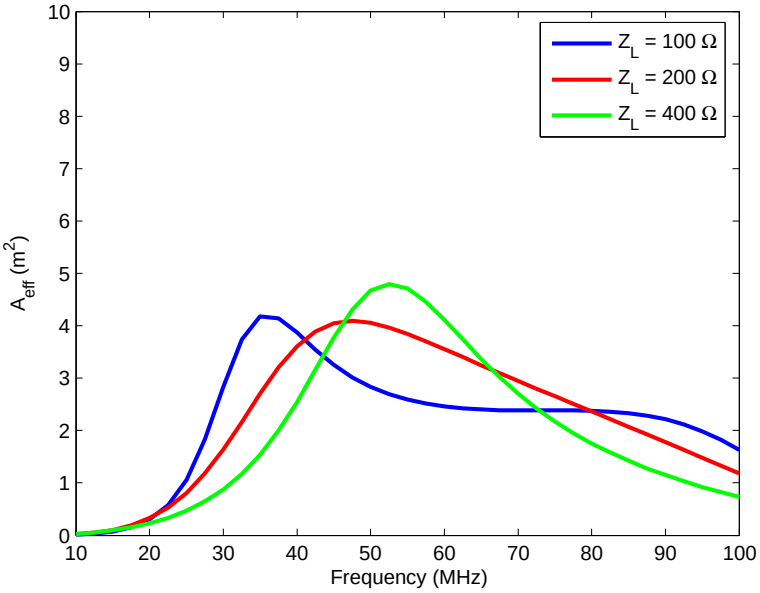

Figure 42: Effective collecting area frequency response at horizon of blade dipole for different values of Z_L.

7 Fork Dipole

The fork dipole, which is also a candidate antenna element design for LWA was originally discussed in [5] and is shown in Figure 43. All of the dimensions provided in [5] have been assumed here with the exception that a shorting braid has been added at the bottom of each element in order to suppress a perturbation in the response near 60 MHz that was exhibited in the original design [6]. As mentioned in [5] a thick wire braid with a radius of approximately 10 mm was used in the original fork design and is assumed here.

The NEC model used to simulate the fork dipole is shown in Figure 44. The calculated metrics for the fork dipole are provided in Figures 45-53 and Tables 13-15 in the remainder of this section.

Figure 43: The fork antenna (without shorting braid across the bottom of each element). Photo obtained from [5].

While the fork dipole achieves a reasonable bandwidth for which T_{ANT} is $>$ 1000K using $Z_L = 100$ Ω, the bandwidth is increased significantly to 22.4 to 83.3 MHz using $Z_L = 200$ Ω, which covers most of the LWA band and is slightly better than the blade dipole for this value of T_{ANT}.

Overall, the patterns for the fork dipole are very similar the those of the blade dipole. The nulls between the mainlobe and sidelobes at higher frequencies are somewhat reduced for the fork dipole as compared with the blade dipole ($<$ 3 dB down from peak for frequencies $\leq$ 80 MHz), however, which improves the calculated beamwidth of the fork dipole at those frequencies. Additionally, the maximum axial ratio for the fork dipole is lower than that of the big blade over all frequencies. For example, the improvement at 74 MHz is 29 %.

The frequency response of the effective collecting area at the zenith of the fork dipole is very similar to the blade dipole. Assuming $Z_L = 200$ Ω, the collecting area of the blade dipole is somewhat higher below 67.5 MHz, while that of the fork dipole is higher at higher frequencies. Like the blade dipole, the transmit based calculation of effective area is higher than the receive based calculation for the fork dipole by up to 14.1 %.

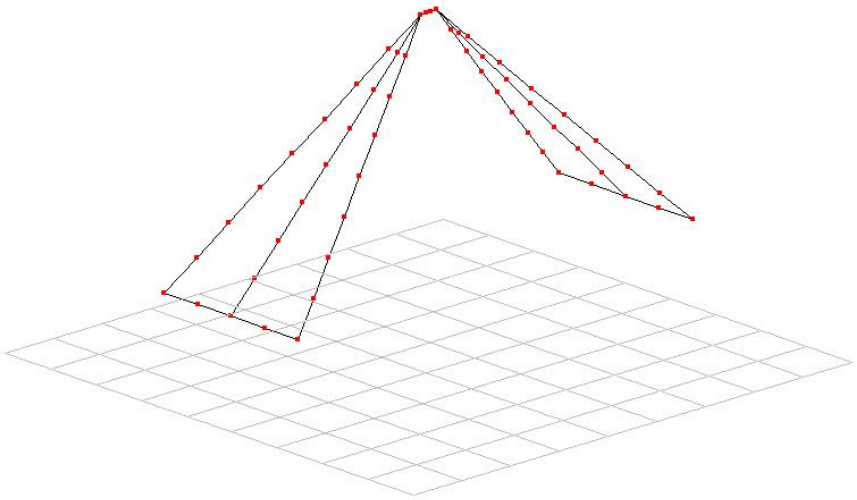

Figure 44: The NEC model used for the fork dipole.

While the frequency response of the sensitivity to vertically polarized signals at the horizon is similar between the two types of antennas, the levels achieved by the fork dipole are lower by a factor of up to nearly two than those of the blade dipole.

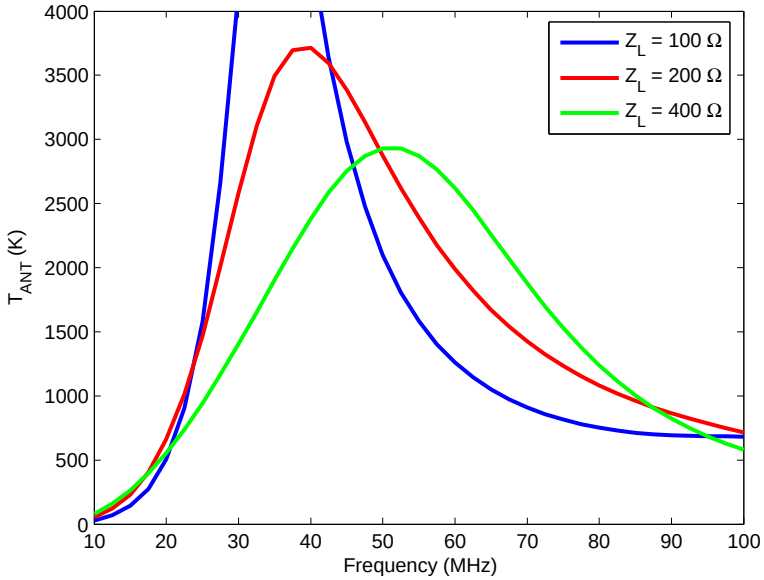

Figure 45: Sky noise frequency response of fork dipole for different values of Z_L.

Table 13: Frequency ranges (in MHz) over which given values of T_{ant} are achieved with fork dipole for different values of Z_L.

	$T_{ANT} > 500$ K	$T_{ANT} > 1000$ K	$T_{ANT} > 1750$ K	$T_{ANT} > 2500$ K
$Z_L = 100\ \Omega$	19.9 -100.0	22.8 - 66.6	25.4 - 53.1	27.1 - 47.4
$Z_L = 200\ \Omega$	18.4 -100.0	22.4 - 83.3	26.3 - 63.7	29.6 - 53.8
$Z_L = 400\ \Omega$	19.1 -100.0	25.6 - 85.1	33.5 - 71.8	41.4 - 61.7

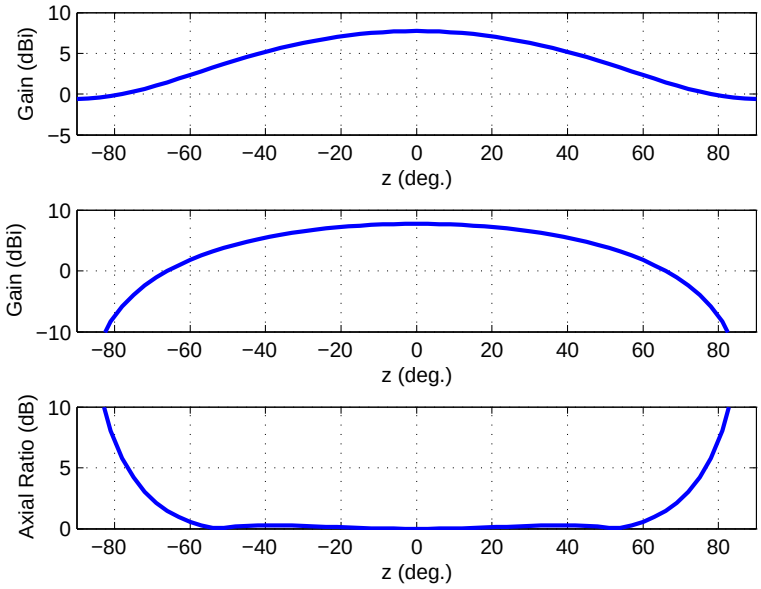

Figure 46: Co-polarized radiation patterns in E-plane (top) and H-plane (middle), and axial ratio (bottom) of fork dipole at 10.0 MHz.

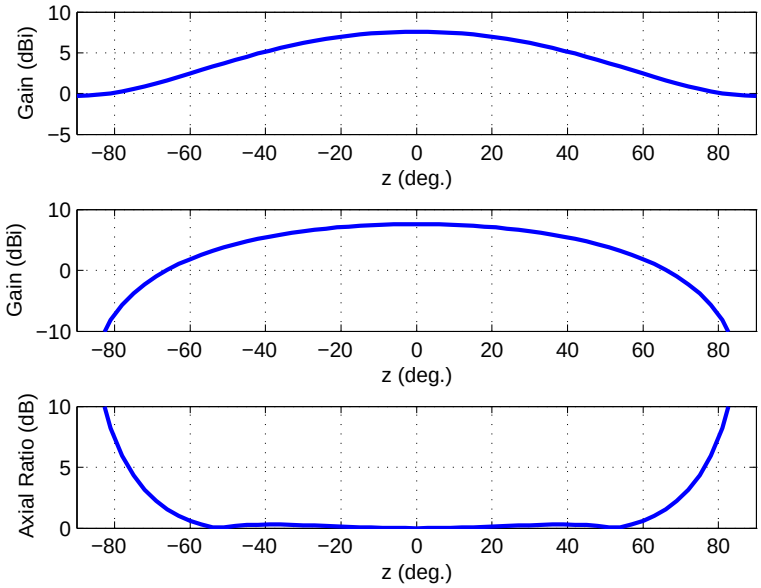

Figure 47: Co-polarized radiation patterns in E-plane (top) and H-plane (middle), and axial ratio (bottom) of fork dipole at 20.0 MHz.

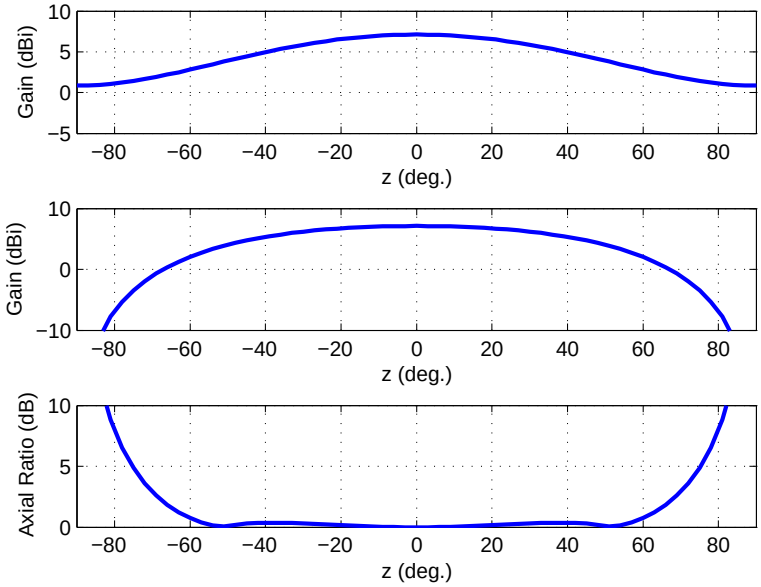

Figure 48: Co-polarized radiation patterns in E-plane (top) and H-plane (middle), and axial ratio (bottom) of fork dipole at 38.0 MHz.

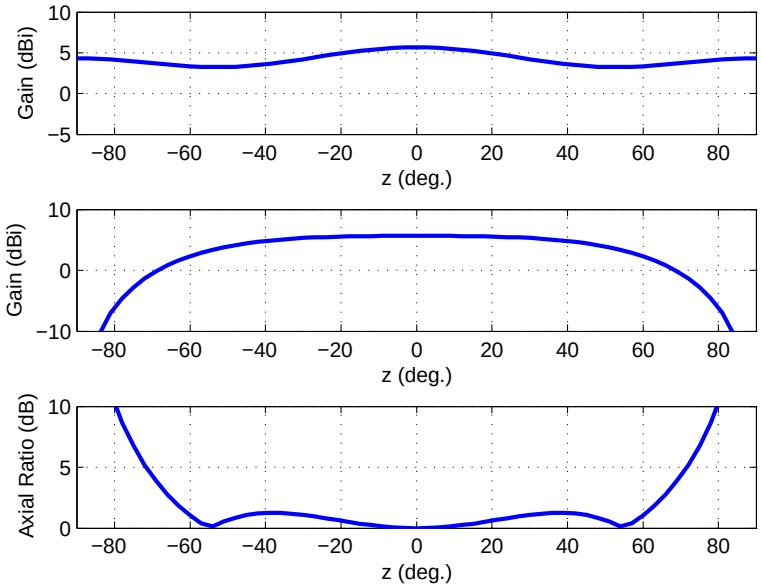

Figure 49: Co-polarized radiation patterns in E-plane (top) and H-plane (middle), and axial ratio (bottom) of fork dipole at 74.0 MHz.

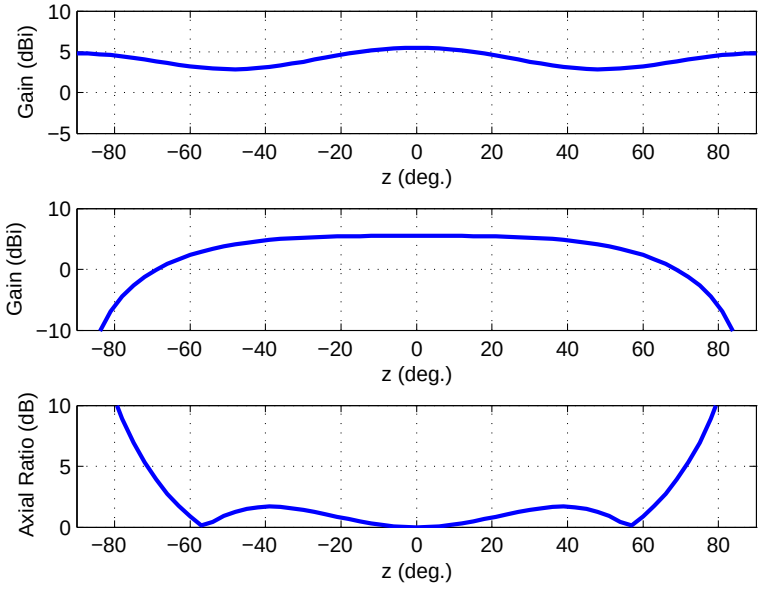

Figure 50: Co-polarized radiation patterns in E-plane (top) and H-plane (middle), and axial ratio (bottom) of fork dipole at 80.0 MHz.

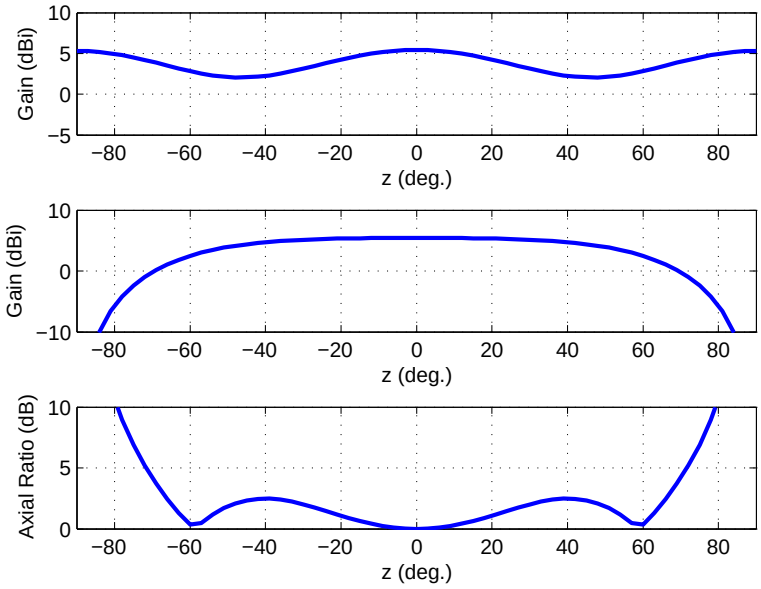

Figure 51: Co-polarized radiation patterns in E-plane (top) and H-plane (middle), and axial ratio (bottom) of fork dipole at 88.0 MHz.

Table 14: Half-power beamwidth in principal planes at different frequencies for fork dipole.

Freq (MHz)	E-plane HPBW (deg)	H-plane HPBW (deg)
10.0	87.0	90.5
20.0	88.7	92.2
38.0	96.4	98.7
74.0	180.0	116.3
80.0	180.0	118.3
88.0	74.6	120.5

Table 15: Maximum axial ratio for $z \leq 74^\circ$ for fork dipole.

Freq (MHz)	max. AR (dB)
10.0	4.2
20.0	4.3
38.0	4.9
74.0	6.8
80.0	6.9
88.0	6.9

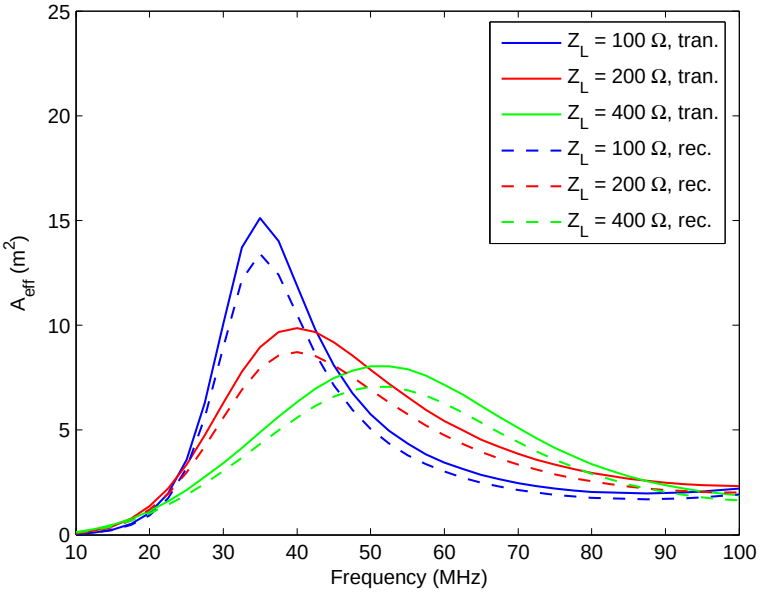

Figure 52: Effective collecting area frequency response at boresight of fork dipole for different values of Z_L.

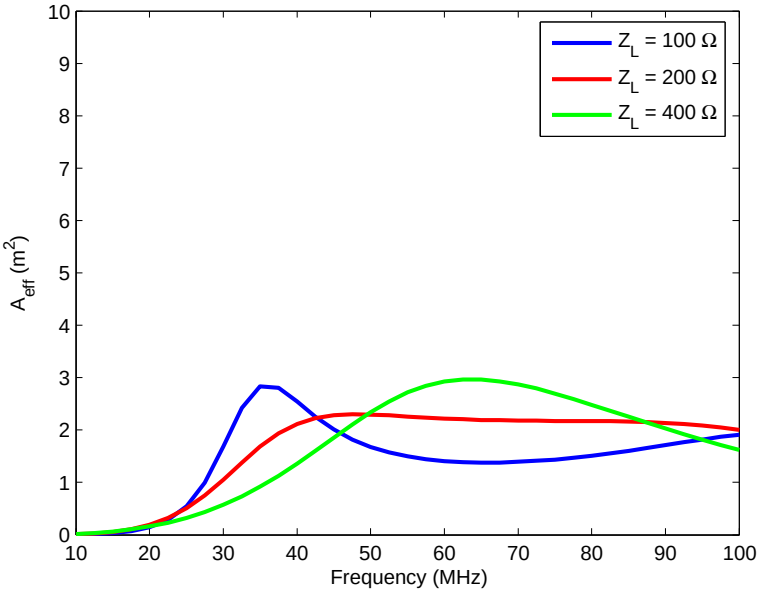

Figure 53: Effective collecting area frequency response at horizon of fork dipole for different values of Z_L.

8 Comparison of Designs

Plots are provided in this section for each metric, which compare the responses of all the antenna designs considered in this report.

If the pre-amp input impedance is constrained to be a low value such as 100 Ω, the broadband dipoles considered offer significantly better sky noise bandwidth than do the wire inverted-V dipoles. The blade dipole and MWA dipole sky noise responses are nearly identical having $T_{ANT} > 1000$ K between 20.3 to 75.6 MHz and 20.4 to 72.6 MHz, respectively. The bandwidth of the fork dipole is slightly reduced with $T_{ANT} > 1000$ K between 22.8 to 66.6 MHz. Even with the thick wire inverted-V dipole, the bandwidth achieved is only 27.5 to 50 MHz.

However, when paired with the optimal value of Z_L the results are somewhat different. Though the blade dipole offers higher values of T_{ANT} over most the band, the fork and MWA dipoles offer slightly better bandwidths for $T_{ANT} > 1000$ K (19.8 to 84.6 MHz for the MWA dipole, 22.4 to 83.3 MHz for the fork dipole, and 20.0 to 77.9 MHz for the blade.) When paired with $Z_L = 400$ Ω, the thick wire dipole achieves $T_{ANT} > 1000$ K over 25.3 to 73.9 MHz, which is a significant portion of the LWA band.

The radiation patterns of the MWA dipole are clearly much different and worse than those of the other antennas as discussed in Section 5. The patterns of the remaining antennas exhibit similar properties over all frequencies. Particularly at lower frequencies ≤ 38 MHz, it is difficult to discern any significant differences. For frequencies ≥ 74 MHz, all of the antennas exhibit sidelobes. However, the fork dipole appears to be the best in terms of the ratio of mainlobe to sidelobe levels and the depth of the null between the mainlobe and sidelobe. The blade appears to be the worst in both regards. These characteristics cause the calculated beamwidth of the fork to be much higher at 80 MHz than the other antennas. Excepting the MWA dipole, all of the antennas have low axial ratio values for $|z| \leq 60°$, especially at or below 80 MHz. The fork and thin wire inverted-V dipoles give the best axial ratio for $|z| > 60°$ for all frequencies. The blade dipole typically exhibits the worst axial ratio for higher zenith angles.

The MWA dipole has the highest effective collecting area at the zenith over all frequencies and for both values of Z_L. This is due to the wideband matching and higher directivity patterns that this dipole exhibits. Having a higher directivity implies that the collective area at angles away from the zenith, however, will be reduced compared to antennas with wider pattern beamwidths. For $Z_L = 100$ Ω, the blade and fork dipoles both provide high collecting area over a wide frequency range, though the values of the blade are somewhat higher. The wire dipoles exhibit high peak collecting area near their half-wave resonance, but very low values at other frequencies. With the best value of Z_L, the blade dipole offers the highest collecting area (besides the MWA antenna) below 60 MHz, while the fork dipole is somewhat better at higher frequencies. The collecting areas of the wire dipoles are still much worse at lower frequencies, though that of the thick wire version with $Z_L = 400$ Ω is much more comparable at higher frequencies to the fork and blade dipoles.

For both values of Z_L, the blade dipole gives the highest sensitivity to vertically polarized signals at the horizon over nearly all frequencies. This is due to the higher sidelobes in the blade dipole radiation patterns, which were noted in Section 6. On the other hand, the MWA dipole exhibits much lower sensitivity than other antennas over nearly all frequencies for both values of Z_L due to the nulls it exhibits at the horizon in the E-plane as discussed in Section 5. With $Z_L = 100$ Ω the wire dipoles exhibit high sensitivity near their half-wave resonance, but much lower sensitivity at other frequencies. The sensitivity of the fork dipole is lower than the blade dipole, but higher than the wire dipoles at frequencies away from the wire dipole resonances. When the best value of Z_L is used, the sensitivity of the fork dipole is greater than the thin wire inverted-V dipole, but less

than the thick wire version.

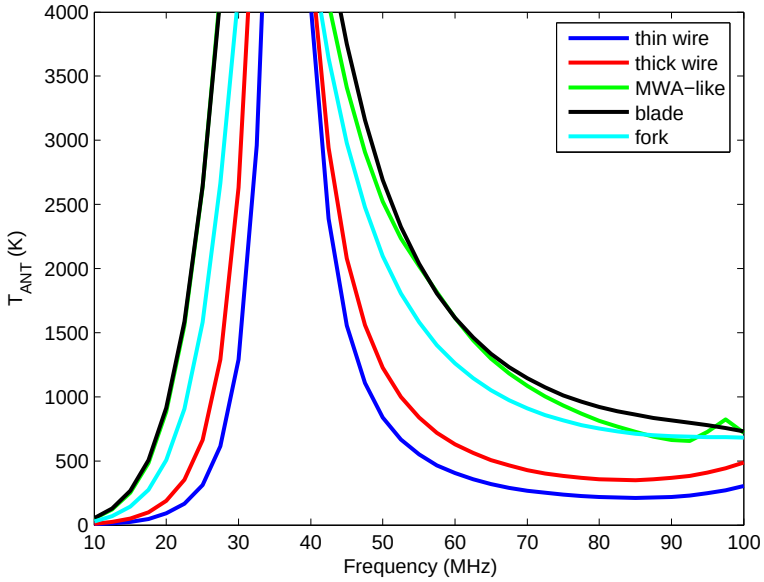

Figure 54: Sky noise frequency response of all antennas for $Z_L = 100\ \Omega$.

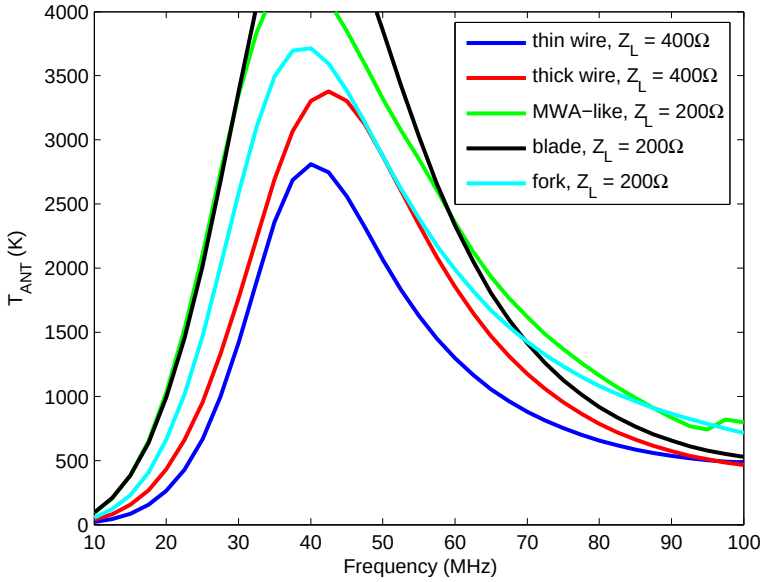

Figure 55: Sky noise frequency response of all antennas with best value of Z_L for each.

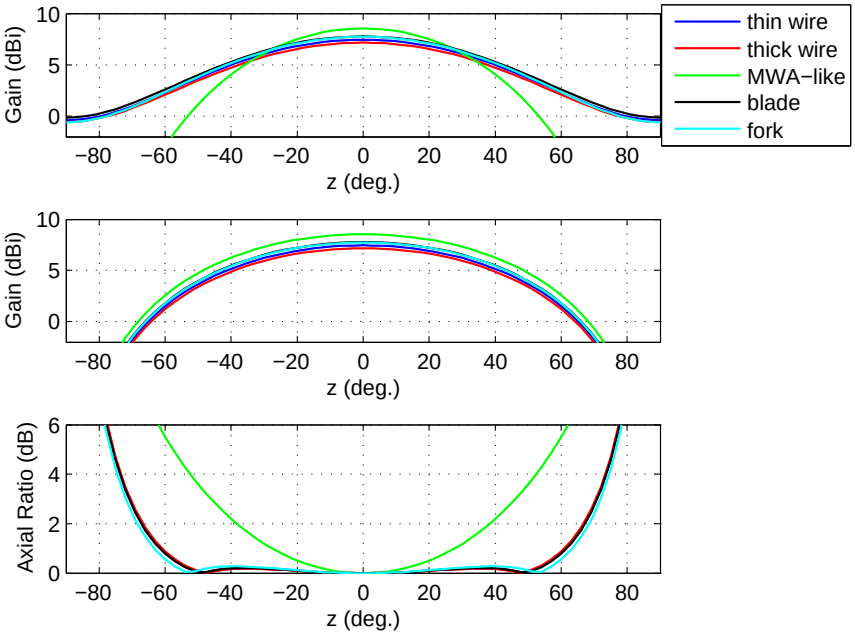

Figure 56: Co-polarized radiation patterns in E-plane (top) and H-plane (middle), and axial ratio (bottom) of all antennas at 10.0 MHz.

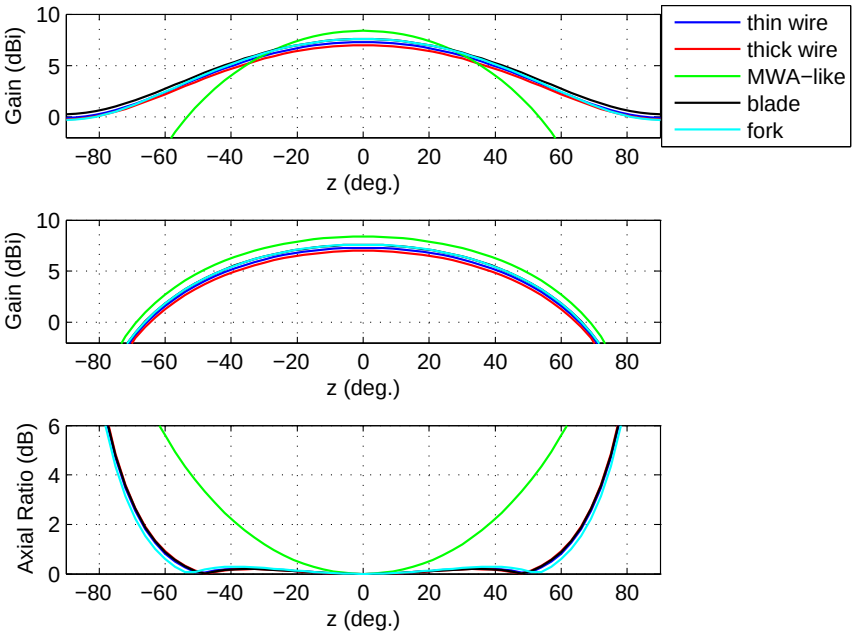

Figure 57: Co-polarized radiation patterns in E-plane (top) and H-plane (middle), and axial ratio (bottom) of all antennas at 20.0 MHz.

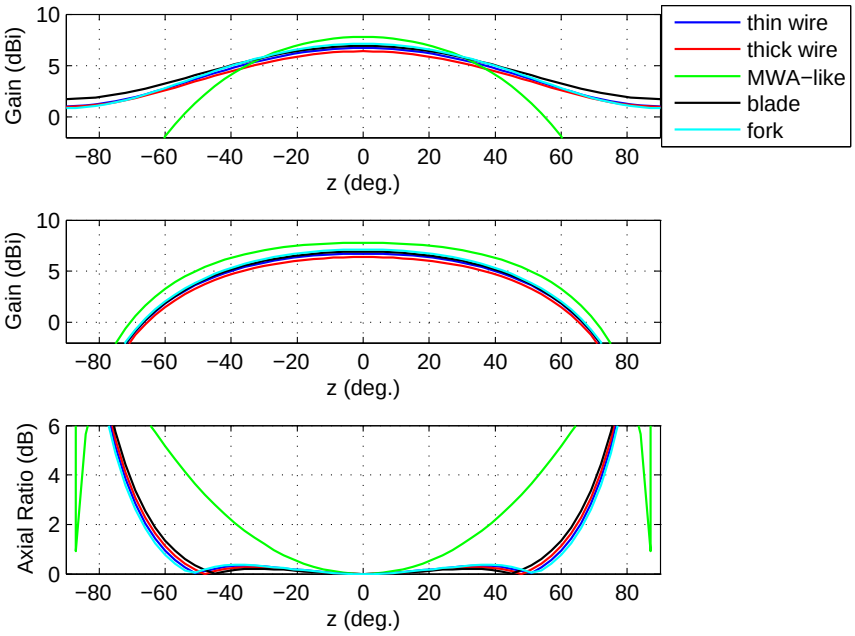

Figure 58: Co-polarized radiation patterns in E-plane (top) and H-plane (middle), and axial ratio (bottom) of all antennas at 38.0 MHz.

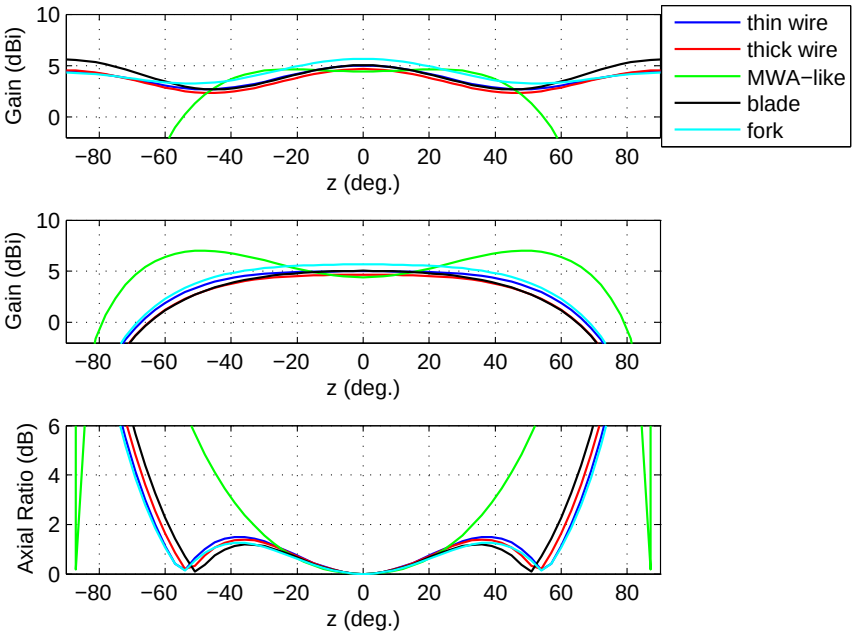

Figure 59: Co-polarized radiation patterns in E-plane (top) and H-plane (middle), and axial ratio (bottom) of all antennas at 74.0 MHz.

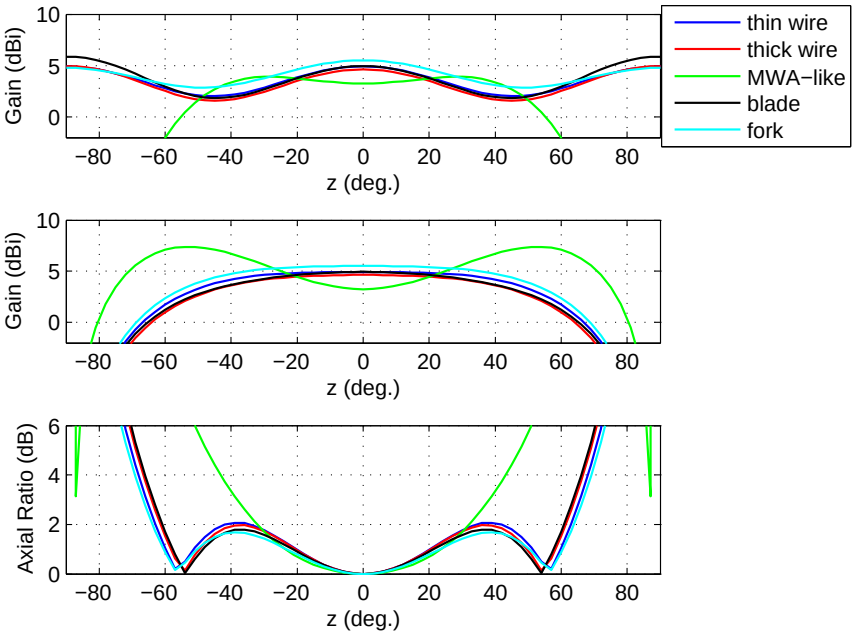

Figure 60: Co-polarized radiation patterns in E-plane (top) and H-plane (middle), and axial ratio (bottom) of all antennas at 80.0 MHz.

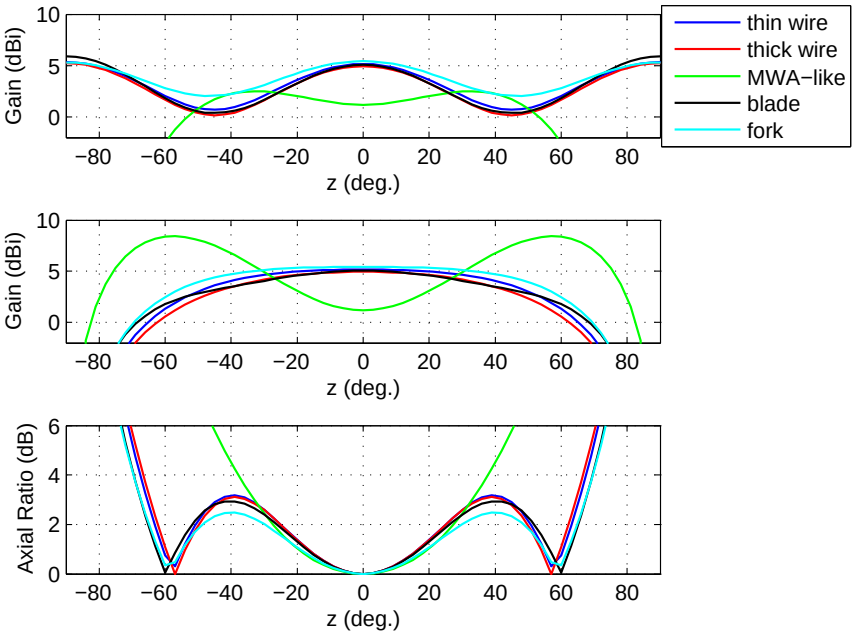

Figure 61: Co-polarized radiation patterns in E-plane (top) and H-plane (middle), and axial ratio (bottom) of all antennas at 88.0 MHz.

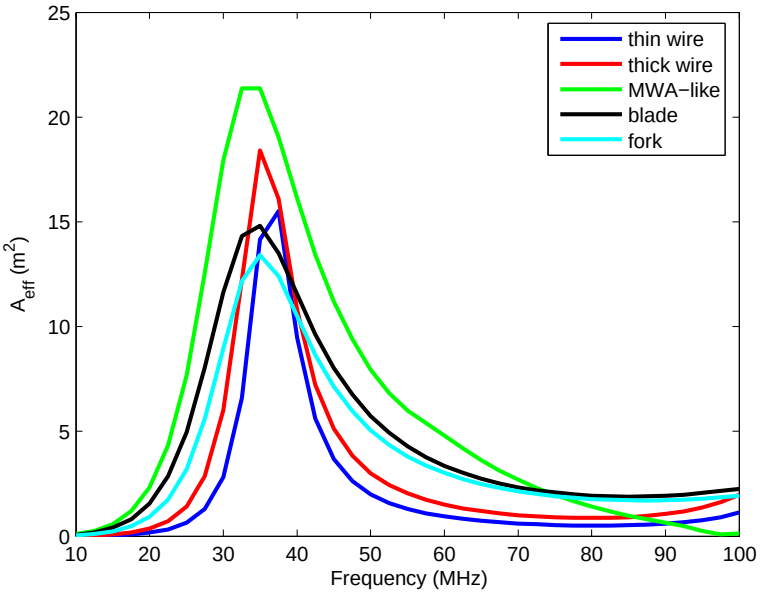

Figure 62: Effective collecting area frequency response at boresight of all antennas for $Z_L = 100$ Ω. Note that receive based calculation used.

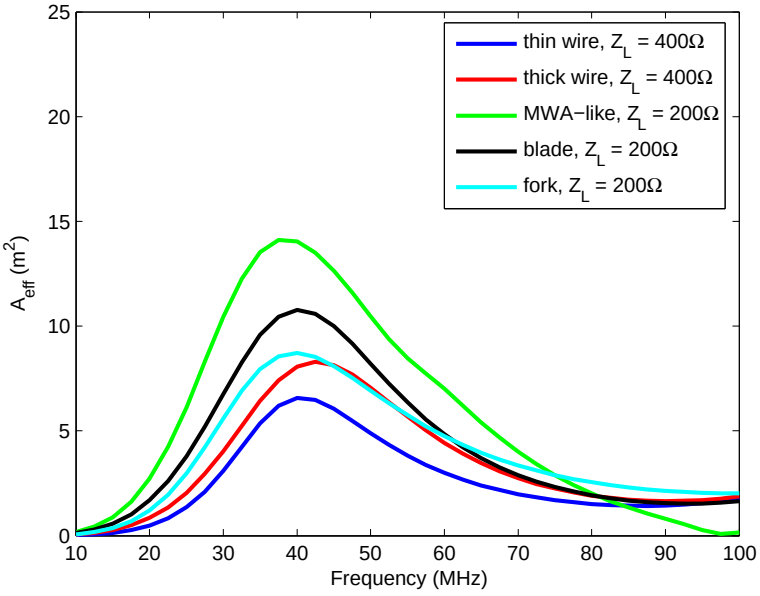

Figure 63: Effective collecting area frequency response at boresight of all antennas with best value of Z_L for each. Note that receive based calculation used.

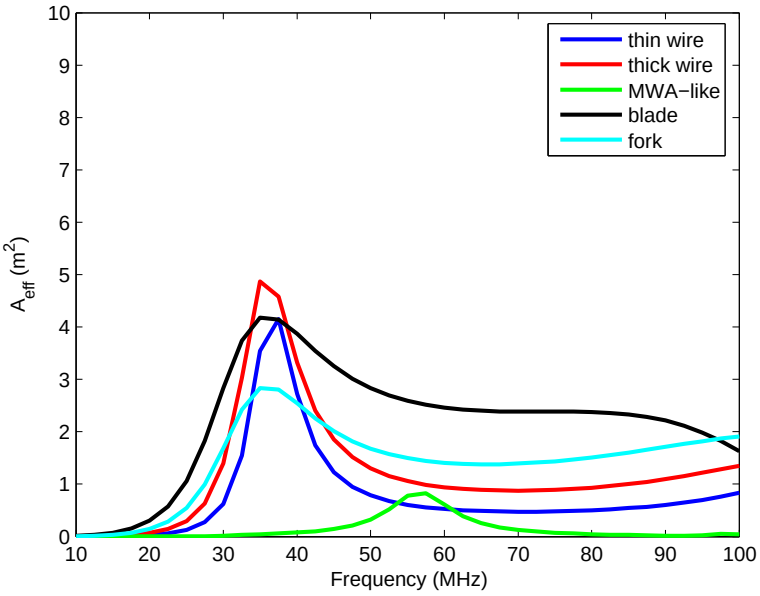

Figure 64: Effective collecting area frequency response at horizon of all antennas for $Z_L = 100\ \Omega$.

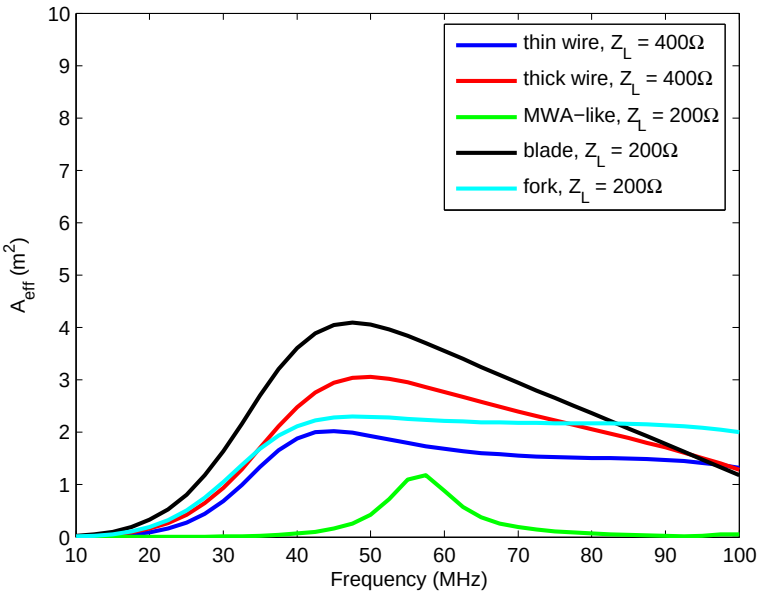

Figure 65: Effective collecting area frequency response at horizon of all antennas with best value of Z_L for each.

9 Conclusions

It should be emphasized that no attempt has been made here to optimize the performance of any of the designs considered. Certainly the performance of each design could be improved in terms of at least one performance metric at a time by changing its design parameters. Additionally, simplifying assumptions have been made in using an infinite PEC ground and ignoring mutual coupling in this analysis. Despite these limitations, it is felt that some basic conclusions can be drawn from the results presented in this report, and are given below.

- If a 100 Ω active balun input impedance is used, the blade and MWA dipoles provide the best sky noise bandwidth, while the bandwidth of the fork is somewhat less. The bandwidths of the wire inverted-V dipoles considered are much less, and are not suitable given the active balun noise temperatures being considered for LWA (175 K to 250 K).
- If reasonable active balun noise temperatures can be maintained with higher input impedance values, the sky noise bandwidths of the blade and fork dipoles can be improved somewhat, and that of the thick wire inverted-V dipole can be improved significantly to cover a large portion of the LWA band.
- The radiation patterns of the MWA dipole exhibit very low E-plane beamwidths at low frequencies and very high axial ratio values over most frequencies, and therefore are unacceptable for use in the LWA. The radiation patterns of the remaining antennas are reasonable and exhibit similar characteristics over the LWA band. Out of these antennas, the patterns of the fork dipole are somewhat better than the rest, and those of the blade dipole are somewhat worse than the rest in terms of the levels of sidelobes and nulls that appear in the patterns at higher frequencies.
- The fork and blade dipoles offer high values of effective collecting area at the zenith over a wide range of frequencies, though the blade dipole values are generally somewhat higher. If a low active balun input impedance is used, wire dipoles offer high collecting area only near their half-wave resonance frequency. If this impedance can be increased, the collecting area of the wire dipoles can be increased significantly at other frequencies.
- The blade dipole generally exhibits the highest sensitivity to vertically polarized signals incident at the horizon. The relative sensitivity between the fork dipole and the thick wire inverted-V dipole is dependent upon the active balun input impedance used.

Given these conclusions, it is recommended that future antenna studies be focused on blade and fork dipole antennas. If it is possible to achieve reasonable active balun performance with higher input impedance values (400 Ω or more), then the thick wire dipole should be added to this list.

The simplifying assumptions made in this study should be removed in future studies. For instance, all calculations should be repeated having replaced the infinite PEC ground with a realistic ground screen in the simulation. This will provide much more realistic radiation pattern calculations and will include ground loss effects. It is also important to consider the effect of mutual coupling on antenna performance. Mutual coupling between two antennas can be calculated by simulation using the techniques described in [7]. Additionally, a method for simulating the performance of a large phased array assuming a particular antenna element design is described in [8]. These methods could be used to compare the mutual coupling characteristics of different antenna designs.

Although useful for relative comparisons between different antenna designs, the effective collecting area calculation provided in this report is difficult to relate to the calibratibility requirement for

LWA. In future studies, the expression provided in [9] to calculate the number of antenna elements needed to calibrate the LWA could be used to compare different candidate designs.

Finally, it was noted that the receive and transmit based calculations of effective collecting area for a given antenna design generally give different results. The amount of difference between the calculations varies significantly between designs. Additionally, the calculation that gives the highest value of collecting area is not consistent among all designs; that is, the receive calculation does not always predict a higher collecting area than the transmit calculation, nor vice versa. Further effort should be spent to better understand these results.

References

[1] H.V. Cane, "Spectra of the Non-Thermal Radio Radiation from the Galactic Polar Regions", *MNRAS*, Vol. 189, p. 465, 1979.

[2] S. Ellingson, "Use of NEC-2 to Calculate Collecting Area", *LWA memo No. 65*, Dec. 27, 2006.

[3] photo obtained from http://www.lofar.nl/photos .

[4] photo obtained from http://www.haystack.mit.edu/ .

[5] N. Paravastu, B. Hicks, P. Ray, W. Erickson, "A New Candidate Active Antenna Design for the Long Wavelength Array", *LWA memo No. 88*, May 30, 2007.

[6] Psersonal communication with N. Paravastu, July 12, 2007.

[7] A. Kerkhoff, "The Calculation of Mutual Coupling Between Two Antennas and its Application to the Reduction of Mutual Coupling Effects in a Pseudo-Random Array", *pending memo.*

[8] S. Ellingson, "A Design Study Comparing LWA Station Arrays Consisting of Thin Inverted-V Dipoles", *LWA memo No. 75*, Jan. 28, 2007.

[9] S. Ellingson, "System Parameters Affecting LWA Calibration (Memo 52 Redux)", *LWA memo No. 94*, July 20, 2007.